Modal Structure Imbalance Fault Detection For Rotating Machines

by

Brendan Smith

A thesis submitted in partial fulfillment of the requirements for the degree of

Master of Science

in

Control Systems

Department of Electrical and Computer Engineering
University of Alberta

Abstract

Fault detection methods have become an important tool in the prevention of safety and reliability issues for industrial rotating machines. Faults in these machines often develop progressively and are not easily observed under operating conditions until severe damage has occurred and further damage during the shut-down process is unavoidable. This type of fault is common in centrifugal separators, where nozzle plug imbalance faults occurring at supercritical operating speeds can lead to catastrophic failure during coast-down after the fault has progressed to the point that an alarm is triggered.

This thesis presents a vibration-based subspace fault detection method intended for detecting rotor imbalance faults. This output-only method detects rotor imbalance faults using an asymptotic local approach that is sensitive to small changes in modal structure. The method was originally developed for stationary structures but is adapted here for constant-speed rotating systems. The faults of interest are static and dynamic rotor imbalances representative of the nozzle plug faults experienced by centrifugal separators.

Two physical models of an idealized centrifugal separator are also presented and used to demonstrate the subspace fault detection method. The first is a mechanical simulation based on rigid body and flexible rotor dynamics derived from finite element analysis of a physical rotor. A physical laboratory bench model based on the simulated machine is also presented that allows the detection method to be demonstrated on a realistically complex system with limited instrumentation.

Subspace fault detection results are presented for both machines using a range of static and dynamic imbalances of increasing severity. For comparison, results are also presented for two alternative detection methods for vibration faults that have received recent attention: sinusoidal synthesis and the Hilbert-Huang Transform. These results demonstrate that the subspace method produces superior results for imbalance faults, particularly in the case of dynamic imbalance.

For Scarlet

A vibrant dog, filled with joy and affection,

who passed away shortly after this thesis was written.

Acknowledgements

I would like to thank my supervisor, Dr. Qing Zhao, whose support and insight were the foundation of this research. I would like to thank my fellow students in the control systems group, in particular Gang Li for his work on the CRD project, and Harry Singh for writing the software interface for my laboratory apparatus. I would like to thank Herbert Drexel and the rest of the machine shop technicians for their excellent work turning my designs into a reality.

I would also like to thank my parents and the rest of my family for their unceasing support and encouragement.

Finally, my most heartfelt gratitude goes to my husband David, whose love made this possible.

Contents

List of Figures

List of Tables

List of Symbols and Abbreviations

2DOF	Two Degrees-of-Freedom
AR	Auto-Regressive
DAQ	Data Acquisition Card
EMD	Empirical Mode Decomposition
FEA	Finite Elements Analysis
HHT	Hilbert-Huang Transform
IMF	Intrinsic Mode Function
LTI	Linear Time-Invariant
NSA	Non-Self-Adjoint
ODS	Operational Deflection Shape
PRBS	Pseudo-Random Binary Sequence
PSD	Power Spectral Density
SS	Sinusoidal Synthesis
$1X$	First harmonic of rotational frequency
$2X$	Second harmonic of rotational frequency
Y	Measured output data matrix
n	Number of data samples
F	State-space state transition matrix
H	State-space output matrix

ϵ_k	State noise sequence
υ_k	Measurement noise sequence
H_0	No-fault hypothesis
H_1	Fault hypothesis
θ	System parameter vector
θ_0	No-fault system parameter vector
Λ	Eigenvalue vector
Δ	Diagonal eigenvalue matrix
Φ	Observed eigenvector matrix
$\zeta_n(\theta_0)$	Residual vector
$M(\theta_0)$	Mean residual sensitivity Jacobian matrix
$\Sigma(\theta_0)$	Residual covariance matrix
$\mathcal{N}(\mu, \Sigma)$	Normal distribution with mean μ and covariance Σ
Υ	Unknown fault vector
R_j	Output covariance matrix for lag time j
$\mathcal{O}_{p+1}(\theta_0)$	No-fault extended observability matrix
S	Orthonormal basis vector matrix for $\mathcal{O}_{p+1}(\theta_0)$
$\mathcal{H}_{p+1,q}$	Block-Hankel output data matrix
p	Row order of extended observability matrix
q	Column order of block-Hankel matrix
m	True system order
r_{norm}	χ^2 test statistic from normalized residual vector
T_r	χ^2 test statistic threshold

Chapter 1

Introduction

1.1 Problem Statement

Vibration faults are a major source of safety and reliability issues for industrial rotating machines. Excessive vibration can manifest for a myriad of reasons, including imbalance; shaft misalignment, warping, and cracking; gear cracking; and bearing failure. In addition, many faults develop progressively with relatively subtle changes in observable vibration magnitudes and spectrum until significant damage has occurred [2]. With modern machines now often designed to operate above one or more critical speeds, a fault that has progressed to the point where it is of sufficiently large magnitude to trigger a shutdown may result in catastrophic damage as the machine coasts down through its critical speeds. Industrial machines are also often poorly instrumented. Typically, vibration signals are obtained from accelerometers mounted on the casing and bearing supports, and in some cases a limited number of proximity sensors are available to measure rotor vibration directly. The challenge is therefore to detect subtle imbalance faults despite limited insight into the physical system.

No single fault detection method can provide useful results for the full range of possible machines, faults, and operating conditions. It is necessary to develop methods that are productive for a limited set of potential faults and machine types. This thesis focuses on a particular fault that occurs in large-scale conical plate centrifugal separators: rotor imbalance caused by nozzle plug. Conical plate separators use centrifugal force produced by rotation of the bowl to remove a suspended solid phase from a continuous flow of lighter liquid phase. The centrifugal force draws the solid phase toward the edge of the bowl, where it flows out through nozzles into an external collection system. A common problem with separators occurs when these nozzles plug and the solid material builds up on the inside of the bowl. This results in a rapidly increasing static or dynamic rotor imbalance, building up to severe levels of vibration over a short period of time. Separators often operate above

their first critical speed, so once a nozzle plug fault results in easily observable vibration at operating speed it tends to produce considerably more damaging vibration as the machine coasts down through one or more critical speeds.

Applying fault detection methods to industrial machines is necessarily more difficult than machines designed and operated in a controlled environment, like a laboratory bench apparatus. Industrial machines are often poorly documented, or documentation is not available to the operator. Abstract models of a machine are rarely available. In addition, there can be considerable variation between individual instances of a single design, and changes of behavior over time as a particular machine ages.

1.2 Scope of Research

Available methods for detecting vibration faults tend to fall into two broad categories: time- and frequency-domain filtering methods that do not utilize a system model, and model-based methods. The latter is distinguished by the use of a mathematical model representing the no-fault system to generate a residual signal that quantifies the discrepancy between the model and the actual system based on output measurements collected from the system while in operation. Typically the model is predetermined using knowledge of the physical system or through data-driven system identification techniques, but adaptive methods that identify a system during operation are also possible.

Nozzle plug imbalance faults produce relatively low vibration levels during the initial period of time when the fault is detectable, but severe damage has not yet occurred. They are often difficult to detect during the initial phase using time- or frequency-domain filtering approaches. However, they are characterized by small changes in the modal structure of the rotating machine that may be detected before vibration becomes severe. This thesis proposes a model-based fault detection method based on a modal model of the no-fault machine to detect the small structural changes caused by nozzle plug faults. Static and dynamic imbalance faults are considered, with particular focus on the harder-to-detect dynamic imbalances.

1.3 Summary of Contributions

Two contributions to the field of model-based fault detection for rotating machines are presented in this thesis.

Simulated and physical models of an idealized horizontal rotor machine are presented.

These machines were designed to allow controlled rotor imbalances that simulate the effect of a nozzle plug fault on a centrifugal separator. The simulation uses a combination of rigid body and flexible rotor dynamics obtained from finite element analysis. It is parameterized to allow the introduction of controlled static and dynamic imbalances at specific points in time. The physical apparatus realizes the idealized machine in a laboratory environment. The simulation and physical models are complementary in allowing the development of realistic fault detection systems for known vibration fault types. The simulation allows access to the internal measurements that are difficult to obtain from a physical machine, while the physical model provides more realistic behaviour and instrumentation and provides a means to verify the validity of the simulation results.

A vibration-based fault detection system is proposed based on the detection of small changes in modal structure. This system is suitable for detecting suddenly-occurring static and dynamic imbalance faults at supercritical speeds. It is based on an adaptation of a subspace-based local approach method developed for stationary structures. The proposed detection method is shown to improve detection performance over current time- and frequency-domain fault detection methods, particularly in the case of dynamic imbalances.

Chapter 2

Literature Review

This section presents an overview of existing literature related to rotating machine dynamics, modeling, faults, and fault detection techniques, with a particular focus on rotor imbalance faults.

2.1 Rotating Machine Faults

Rotating machines may experience a broad range of faults. These include static and dynamic imbalances, rotor damage and misalignment, gear damage, bearing damage, and instability caused by bearing or working fluid dynamics. By far the most common method for detecting these faults is through analysis of the vibrations they produce [2, 3]. This thesis is focused on lateral rotor vibration faults caused by imbalance. Rotor imbalance produces vibration at frequencies corresponding to the shaft speed and its harmonics. (These frequencies are often referred to as '1X', '2X', '3X', and so on.) It is often difficult to distinguish vibration produced by imbalance faults from other shaft speed faults, like shaft misalignment and cracking. For the purposes of this thesis only imbalance faults are considered, as they are the most relevant to the nozzle plug imbalance scenario encountered by centrifugal separators that originally motivated this work.

Rotor imbalance is present whenever the principle axis of inertia for the rotor is not coincident with the axis of rotation. Three types of imbalance are possible: static imbalance, couple imbalance, and dynamic imbalance. Static imbalance occurs when the principle axis of inertia is parallel to the axis of rotation, but not coincident. A rotor with static imbalance experiences a centrifugal force perpendicular to the axis of rotation. A couple imbalance occurs when the mass center lies on the axis of rotation and the principal axis of inertia passes through the mass center, but the principal axis is not parallel with the axis of rotation. Couple imbalance, as the name implies, produces a couple moment on the

rotor. A combination of static and couple imbalances is known as a dynamic imbalance. In engineering contexts the latter term is often used for couple imbalances regardless of whether a static imbalance is also present. This is the convention followed in this thesis.

Methods for detecting vibration faults fall into three categories: time-domain filtering methods, frequency-domain filtering methods, and model-based methods [4, 5]. Filtering methods represent well-explored and commonly-applied fields of research [6, 7]. However, the limitations to a purely filtering approach have led to an increased interest in model-based approaches. Obtaining adequate system models for industrial machines is often challenging. Models can be determined by reasoning from physical principles, through data-driven system identification, or a combination of the two [8, 3, 9, 10]. In the simplest cases, models can be derived from design documentation using physical modeling principles. This approach is limited by the complexity of many machines and difficulties obtaining sufficient documentation from the manufacturer. In addition, there may be substantial variation between machines, and over the lifetime of a single machine. Environmental interactions are also an issue, as even when a model is known for the machine itself vibration characteristics may be substantially modified by interaction with the foundation and inlet/outlet connections. A purely theoretical derivation is often impossible in practice. To avoid the problems with theoretical modeling, data-driven techniques may be used. When applied to vibrating systems this is also known as modal analysis. It presents particular challenges in the case of rotating structures.

2.2 Rotordynamics and Modal Analysis

Vibrating systems can be characterized by their modal structure: natural frequencies, mode shapes, and damping coefficients. In the absence of a fault, most stationary structures have a modal structure that does not vary as a function of time or input. Rotating structures are fundamentally different. In a rotating system, gyroscopic forces introduce a time dependency into the equation of motion [11]. If, as is commonly the case, the rotor is isotropic and measurements are taken in an inertial frame of reference, the differential equation of motion is dependent not on time, but on rotational speed.

In a non-rotating system, the system matrices are typically constant in time and symmetric. Such systems are characterized as self-adjoint. For a rotating system the damping and stiffness matrices are not symmetric and the system is described as non-self-adjoint. (NSA) As the equation of motion for a NSA system is speed-dependent, the modal structure for an NSA system is also speed-dependent. At any given constant operating speed,

the system has a unique set of natural frequencies, damping ratios, and mode shapes. In normal operation, the machine must speed up and coast down through a speed range where the instantaneous rotating speed is equal to one or more natural frequencies. Resonance is often observed at these points, which are referred to as critical speeds. It is important to distinguish between natural frequencies, which are a function of speed, and critical speeds, which are a property of the machine as a whole.

If an isotropic NSA rotating system is maintained at a constant operating speed, the equation of motion becomes LTI. As such, the vibrational characteristics of a constant-speed machine can be treated similarly to a stationary structure in many ways. However, because gyroscopic forces act to deform the rotor, natural frequencies and mode shapes of a rotating system behave differently than in stationary systems. There are two main types of mode observed in rotating systems: rigid body modes and whirling modes. Rigid body modes are the result of motion within the bearings, and typically occur at low frequencies when bearing stiffness is not significantly greater than rotor stiffness. They are weakly dependent on rotational speed. Whirling modes occur when the rotor deflects into a plane formed by the rotor and the bearing centreline. It is possible to have whirling modes in the direction of rotation (forward whirling) and in the opposite direction as rotation (backward whirling). Forward whirling increases with rotational speed, while backward whirling decreases. The relevant critical speeds for a machine with a flexible rotor are typically the intersection of operating speed with the first and second whirling modes. It is however possible that backward whirling modes will not be observed if the rotor is axisymmetric and the bearings are isotropic, as rotational energy cannot be fed into the backward modes [11].

Modal analysis of rotating structures is considerably more challenging than stationary structures. In addition to the problem of speed dependence, a rotor is typically much more difficult to instrument and excite than a non-rotating structure. In addition, the degree of asymmetry observed in the rotor, bearings, and foundation determine the extent of excitation and instrumentation required to analyze a particular system. While a simple system with axisymmetric components may be analyzed with a single point of excitation and measurement, asymmetrical systems may in theory require excitation and observation at all points along the rotor [11]. The idealized machines considered in this thesis are axisymmetric to constrain the amount of instrumentation required. Even under these conditions, obtaining a model of the modal structure by analysis of the machine is highly involved. The approach taken in this thesis is to derive the modal structure from simulation and finite element analysis, and then confirm the models by comparison with the complete machines.

2.3 Modal Structure Fault Detection

In response to issues with theoretical modeling, data-driven identification techniques have become popular. One such method is subspace identification. Subspace methods use geometric operations and projections on the row spaces of measured data matrices to infer the internal structure of a system [12]. They are particularly useful for estimating the modal structure of a system, and can be applied to output-only systems with stochastic inputs [13]. Subspace methods have been successfully applied to a range of structural and mechanical applications [14, 15, 16, 17]. Subspace methods may also be adapted to detect changes in modal structure when compared with a no-fault model [18]. This is useful for fault detection because the modal structure of a vibrating system is a direct function of the physical properties of that system. If the mass, damping, or stiffness of a system change, the frequency, damping, or mode shapes of the vibration will also change. Vibration faults can be identified by observing changes in the modal structure of a system [19].

Basseville et al proposed a fault detection technique based on subspace methods that was shown to detect vibration faults in stochastic systems by generating a residual that is sensitive to small changes in the modal structure [18]. This method is based on a local asymptotic approach to the fault detection problem, which rephrases the problem in terms of discriminating between two similar hypotheses by generating a residual whose distribution is known and distinct in both cases [20, 21, 22]. The local approach allows the problem to be transformed from one of identifying and comparing modal structures to the systematic and well-understood statistical problem of monitoring the mean of a Gaussian-distributed vector. The residual vector distribution has a non-zero mean if and only if a fault is present. This method was developed for stationary structures, and has been profitably applied to practical industrial [23] and aeronautical [16] structures. The Basseville subspace-based method is adapted in this thesis for use in constant-speed rotating systems with gyroscopic effects and flexible rotor dynamics.

2.4 Alternative Fault Detection Methods

Two alternative fault detection algorithms were selected for comparison with the subspace method. The first was an autoregressive (AR) frequency estimator method known as sinusoidal synthesis. (SS) A vibration signal produced by a rotating machine can be considered as the combination of a sinusoidal component, an impulsive component associated with certain fault conditions, and noise [24]. Rotating machine fault detection based on AR models

is well-established [25], but a significant drawback is that the AR model must be predetermined from no-fault data. Given the sinusoidal nature of rotating machine vibration, it is possible to determine the model adaptively using a frequency estimator approach, known as sinusoidal synthesis. The SS method implemented for this thesis used a time-domain linear predictor to extract the sinusoidal frequency properties, and predicts future measurements using a sum-of-sinusoids approach based on the estimated sinusoids [26]. The SS method was developed to detect impulsive faults that deviated from the basic sinusoidal character of rotating machine vibration, such as gear crack faults, and has been demonstrated to be effective in this context.

The second alternative method was the Hilbert-Huang transform [27]. (HHT) This method consists of an empirical mode decomposition (EMD) of the vibration signal into near-orthogonal components known as intrinsic mode functions (IMFs), followed by Hilbert transformation of the IMFs to obtain the instantaneous frequency as a function of time, which is then visualized using a time-frequency plot. Each IMF represents a natural oscillatory mode of the signal, and expert analysis of the time-frequency plot often reveals patterns characteristic of particular types of fault associated with particular IMFs. HHT has become a popular alternative to traditional Fourier analysis as HHT may highlight transient effects that are concealed by Fourier transform, particularly in cases where the faults are non-stationary and transient [28, 29].

Chapter 3

Rotating Machine Models

3.1 Simulated Machine Overview

A physical simulation of an idealized rotating machine was built in Simulink to serve as a testbed for the fault detection system described in this paper. This machine was constructed using a combination of rigid-body SimMechanics library blocks and custom Simulink subsystems to simulate bearing and flexible rotor dynamics. A 3D rendering of the machine generated by the SimMechanics visualization package is provided in Figure 3.1

The machine used a ⅜-inch steel shaft two feet in length, driven by an DC motor via a flexible coupling. The shaft was mounted on two oil-impregnated bronze journal bearings, which were supported by aluminum bearing blocks bolted to a heavy aluminum baseplate. Three aluminum flywheels were mounted to the shaft, at the center and at positions on the left and right equidistant from the center flywheel and the bearings. Each flywheel had two concentric rings of holes for the attachment of imbalance weights. Holes were drilled at 30° intervals for the inner ring 3 cm from the axis of rotation, and at 15° intervals for the outer ring, at a distance of 6 cm. Weights could be attached through the holes to create a variety of controlled imbalances. Static imbalances were created by placing a single weight at 0° on the center flywheel, (as pictured in Figure 3.1) while a dynamic imbalance was created with weights at 0° and 180° on the right and left flywheels, respectively. As no practical rotating machine can be perfectly balanced, the simulated machine was configured with a residual 2 g static imbalance at 0° on the center flywheel.

The most common approach to modeling a rotating machine combines a finite element analysis (FEA) model of the shaft as a flexible beam with a linearized bearing model [3, Chapter 2]. The simulation incorporated these elements by embedding custom Simulink subsystems for the rotor and bearing dynamics into a standard SimMechanics model of the machine as a collection of rigid bodies and joints. Figure 3.2 illustrates the highest level

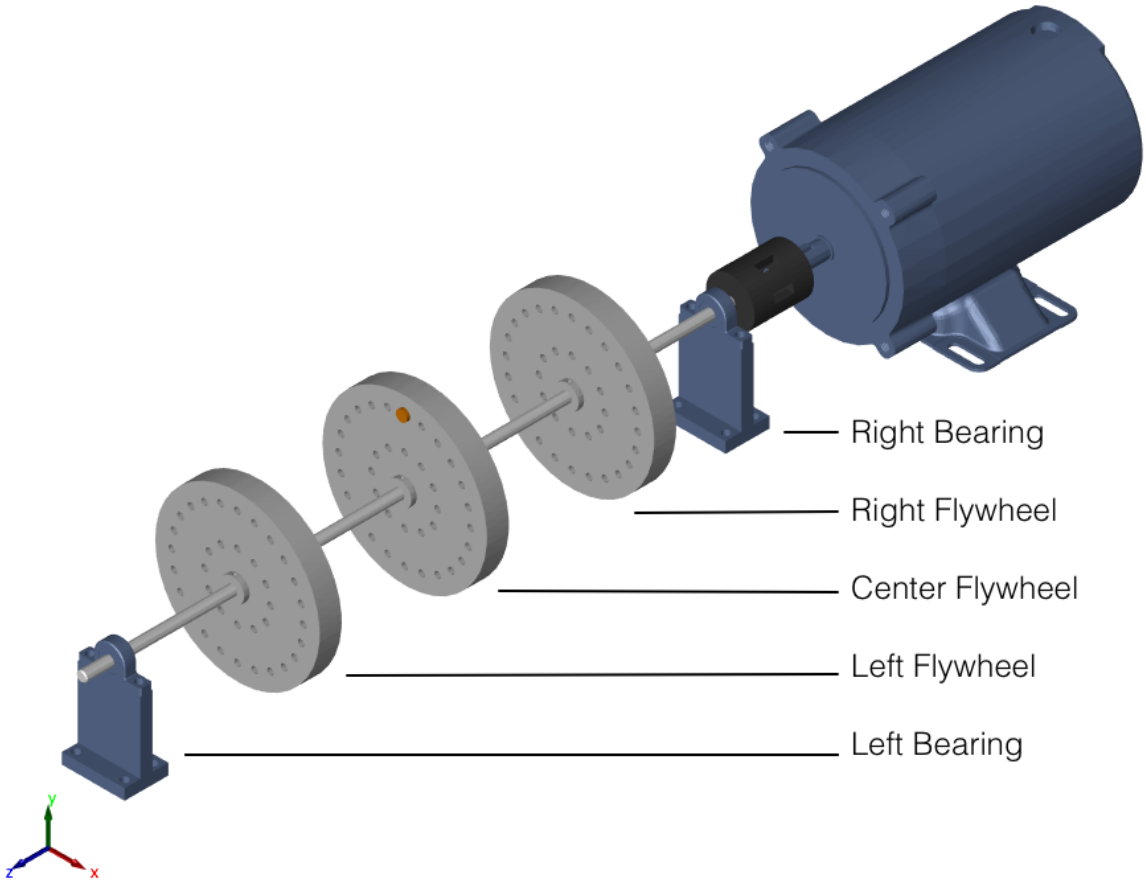

Figure 3.1: Simulated Rotor Imbalance Machine 3D Visualization

of the mechanical model implemented in Simulink. The model had one input, rotor speed in RPM, and eight outputs: x- and y-axis rotor displacement from the axial centerline was measured in mil (one thousandth of an inch) at each bearing and at two positions between from the center flywheel and the outer flywheels.

A continuous-time solver was required to support the physical simulation, but all measurements collected for fault detection were sampled at 1 kHz.

3.1.1 Bearing Model

A linearized two degrees-of-freedom (2DOF) bearing model was used to represent each bearing in Simulink, as illustrated in Figure 3.3. The 2DOF model represents a bearing as a prismatic joint in the X-Y plane with direct and cross-coupled linear spring-and-damper systems for each axis [3, Chapter 5]. Spring and damper coefficients are typically obtained by referencing tables of constants compiled in bearing databooks or identified from data collected from operating machines. The degree of axial symmetry and cross-coupling has

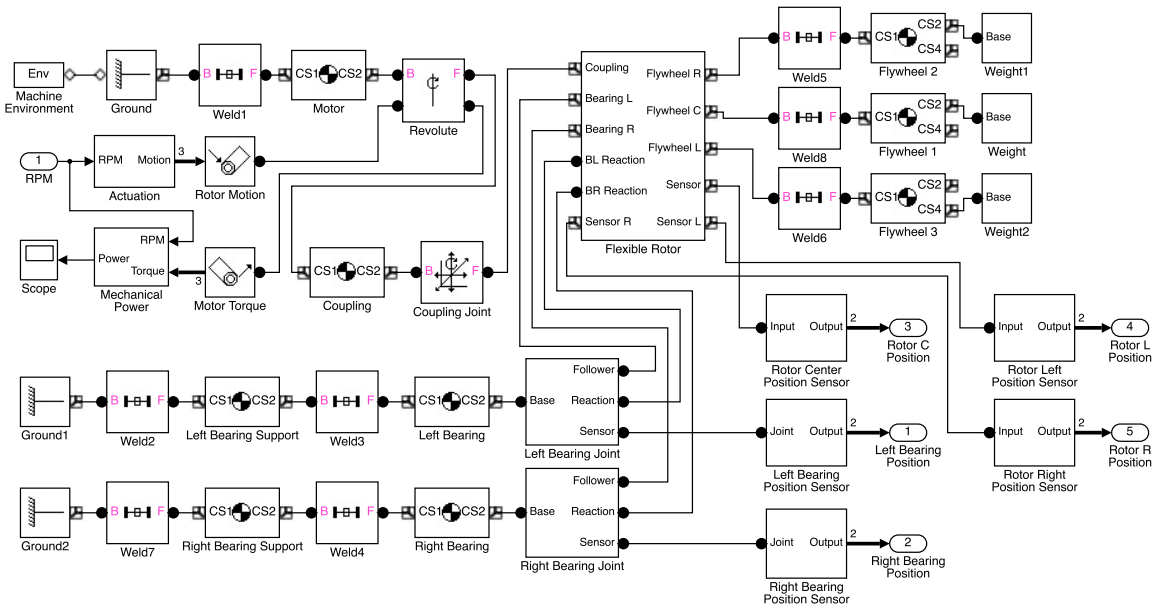

Figure 3.2: Simulink Mechanical Subsystem Diagram

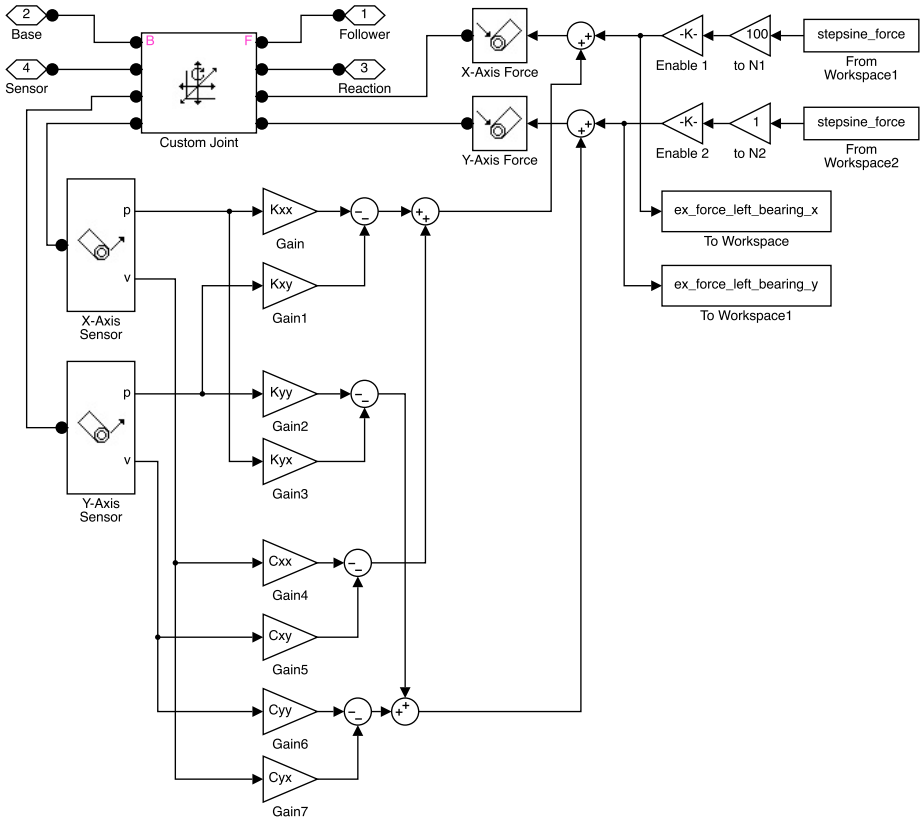

Figure 3.3: Simulink Linearized 2DOF Bearing Subsystem Diagram

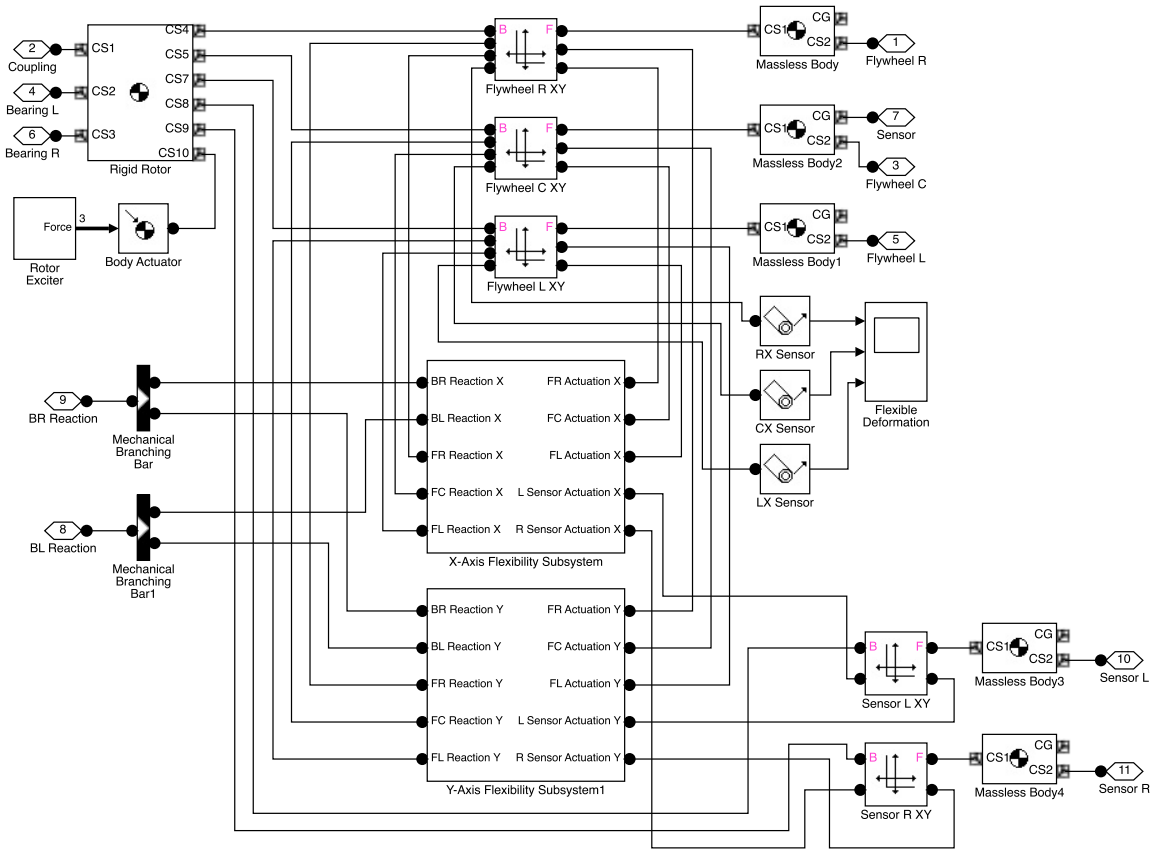

Figure 3.4: Simulink Flexible Rotor Subsystem Diagram

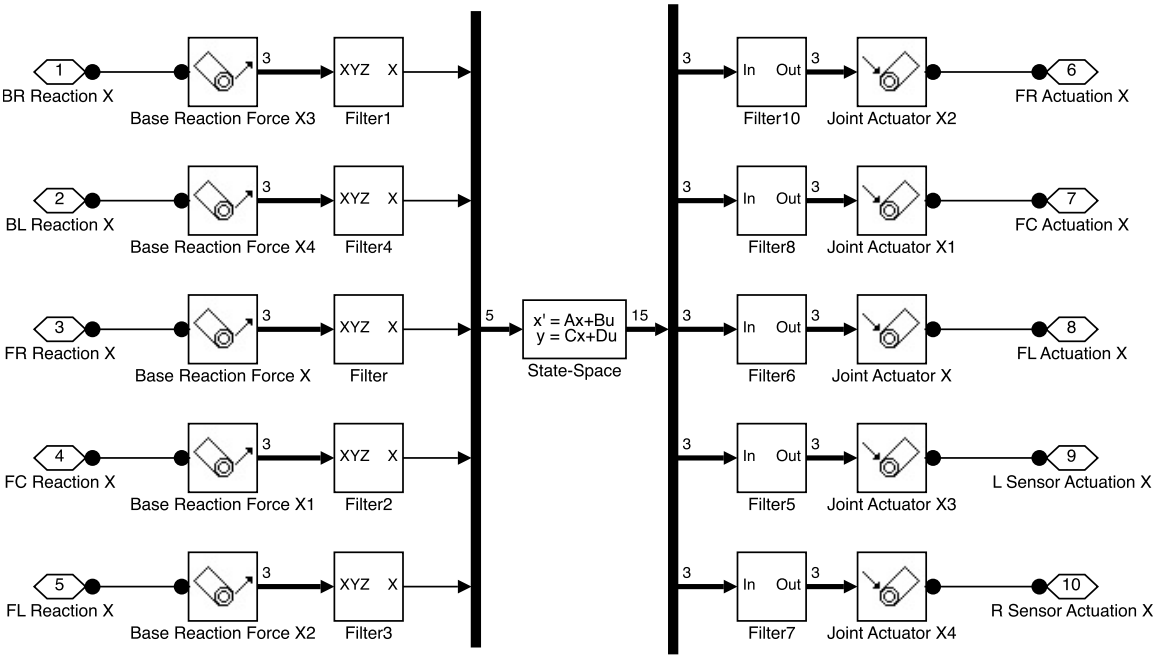

Figure 3.5: Simulink Flexibility Subsystem Diagram

a significant influence on the modal structure of a rotordynamic system. The simulation used simple sleeve bushings, which were modeled as stiff axisymmetric bearings with light damping and no cross-coupling between the translational axes.

3.1.2 Flexible Rotor Model

The SimMechanics block library does not provide a built-in system for simulating flexible bodies. Flexible dynamics can be incorporated into the model using a finite elements approach, as described by Chudnovsky et. al. [1]. This technique encapsulates the flexible body dynamics as a state-space subsystem whose inputs are loads on the body and whose outputs are the flexible deflections relative to the rigid body at specific points of interest, as illustrated schematically in Figure 3.6. A modal analysis of the flexible body is performed in a FEA program to obtain the natural frequencies and mode shapes, which are then used to construct the state-space system as a M-orthogonal modal decomposition of the system as a set of harmonic oscillators. Modal analysis of the rotor was conducted in ANSYS to obtain the first four mode shapes, as shown in Figure 3.7 once normalized to the mass matrix. The nodal displacements at the points of measurement in the simulation for the rigid-body mode and the first flexible mode are listed in Table 3.1, measured in meters and also normalized to the mass matrix. MATLAB scripts based on the Chudnovsky method were used to process the FEA results and obtain a five input, five output state-space system relating loads on the rotor at the bearing and flywheel positions to flexible displacement of the shaft at the three flywheel positions and two rotor position sensors.

Figure 3.4 shows the internal structure of the rotor subsystem in Simulink. Flexible dynamics are integrated into a rigid-body model of the rotor by actuating massless bodies in the X-Y plane at each interface between the rigid rotor and flywheels. Two identical subsystems encapsulate the flexible dynamics separately for the x and y axes. The internal structure of the flexible body subsystems is shown in Figure 3.5. The subsystem consists of five reaction force inputs calculated in the parent subsystem from joint reactions at the flexible interface positions and five absolute motion outputs calculated by the state-space system. The absolute motion outputs are used to actuate massless bodies that represent the position of the deformed body.

3.1.3 Noise

The simulated machine was configured so that additive white noise could be applied to all output signals using Band-Limited White Noise Simulink blocks. A separate noise generator

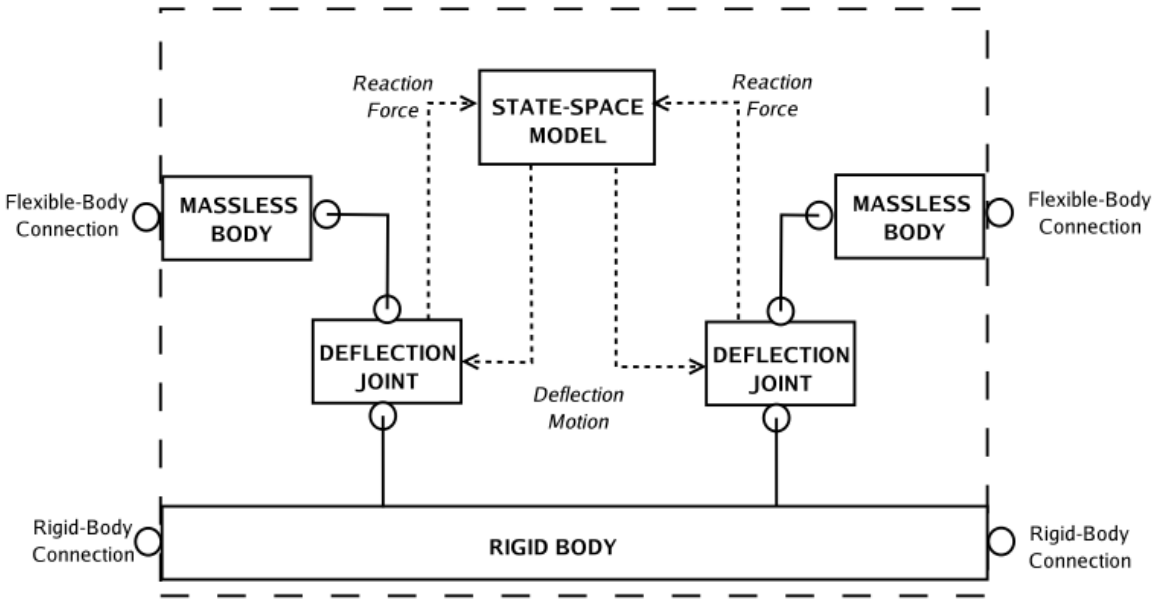

Figure 3.6: Chudnovsky Flexibility Subsystem [1, p. 9]

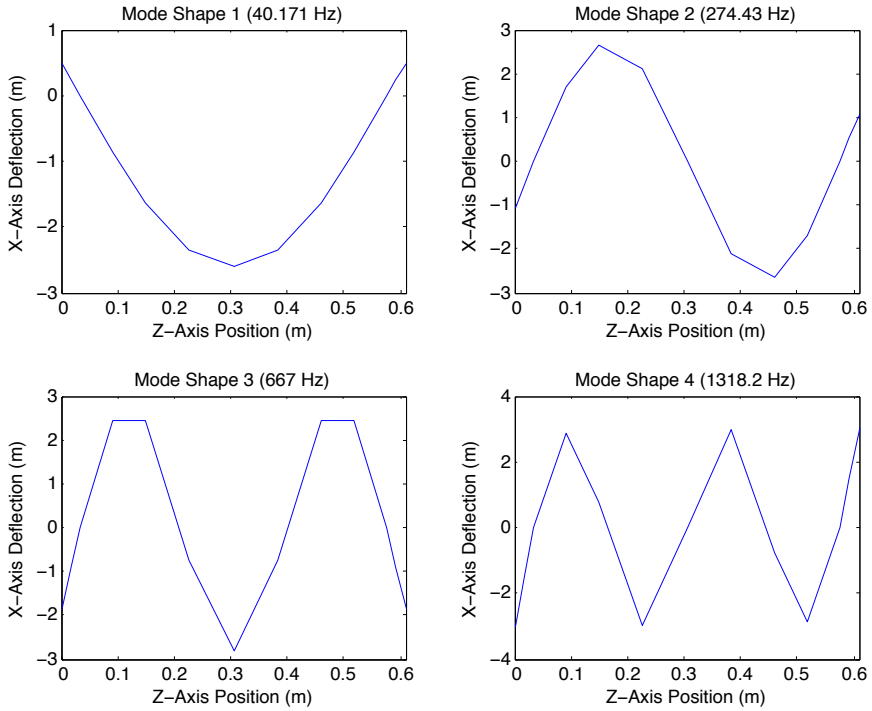

Figure 3.7: First Four Flexible Rotor Mode Shapes Obtained From FEA

Table 3.1: Mode Shape Displacement Obtained From FEA (m)

Mode	L Bearing	L Rotor	C Rotor	R Rotor	R Bearing
Rigid	1.720	1.720	1.720	1.720	1.720
Flex	0	-2.351	-2.609	-2.351	0

was used for each output signal, with a unique random seed but identical power spectral densities (PSD) for all signals of the same type. Position signals (measured in mils) were assigned a PSD of $1\times10^{-4}\ mil^2/Hz$. Rotor speed signals (measured in RPM) were assigned a PSD of $1\times10^{-6}\ RPM^2/Hz$.

3.1.4 Operating Speed

The simulation was designed to allow a variety of rotational speed input signals, including constant speed and pseudo-random binary sequences (PRBS). As a typical centrifugal separator would normally maintain a constant speed except during startup and coast down, rotor speed was held constant at 1000 RPM except when otherwise specified. This speed was chosen to ensure that both the simulated and physical machines were operating comfortably above their first critical speeds. The simulation applied a first-order low-pass filter to the set speed signal to simulate the effect of the speed controller used for the physical system, which limits the rate at which the rotor can accelerate.

3.2 Simulated Machine Vibration Analysis

3.2.1 Vibration Signal Characteristics

Figures 3.8 and 3.9 show detailed selections of the rotor vibration waveforms captured during no-fault simulations. Figure 3.8 contains a 0.2 s segment of the x- and y-axis left rotor position measurements captured during constant-speed operation at 1000 RPM. Vibration is the result of the residual 2 g static imbalance. These vibration signals are characterized by sinusoidal signals with a dominant 1X component. The effect of noise on position measurements can also be observed.

Figure 3.9 demonstrates the effect of varying the speed of rotation using a PRBS speed signal alternating between 975 RPM and 1025 RPM. Transient effects are observed as the rotational speed changes, whereas during periods of constant-speed operation the vibration is dominated by the 1X frequency component, with a magnitude that is determined by the rotational speed.

Figures 3.10 and 3.11 show periodograms for the x-axis left rotor position signals for the constant and PRBS speed inputs, respectively. Both periodograms illustrate the dominance of the 1X frequency, as expected for a residual static imbalance. The pair of peak frequencies in Figure 3.11 are the result of varying between two constant operating speeds when a PRBS speed input is applied.

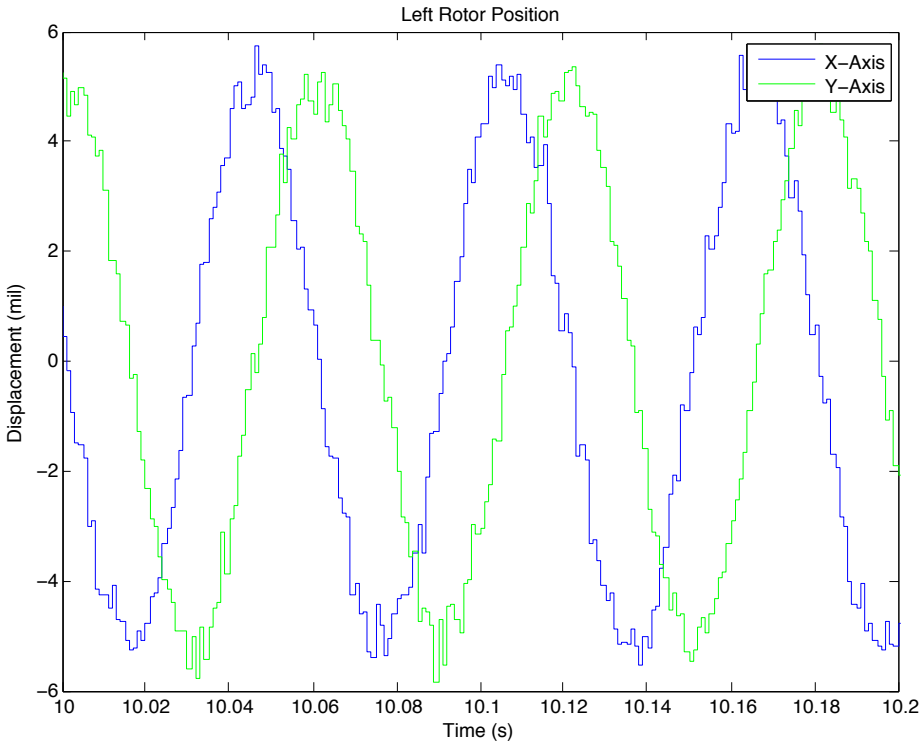

Figure 3.8: Simulated No-Fault Left Rotor Vibration (Detailed View)

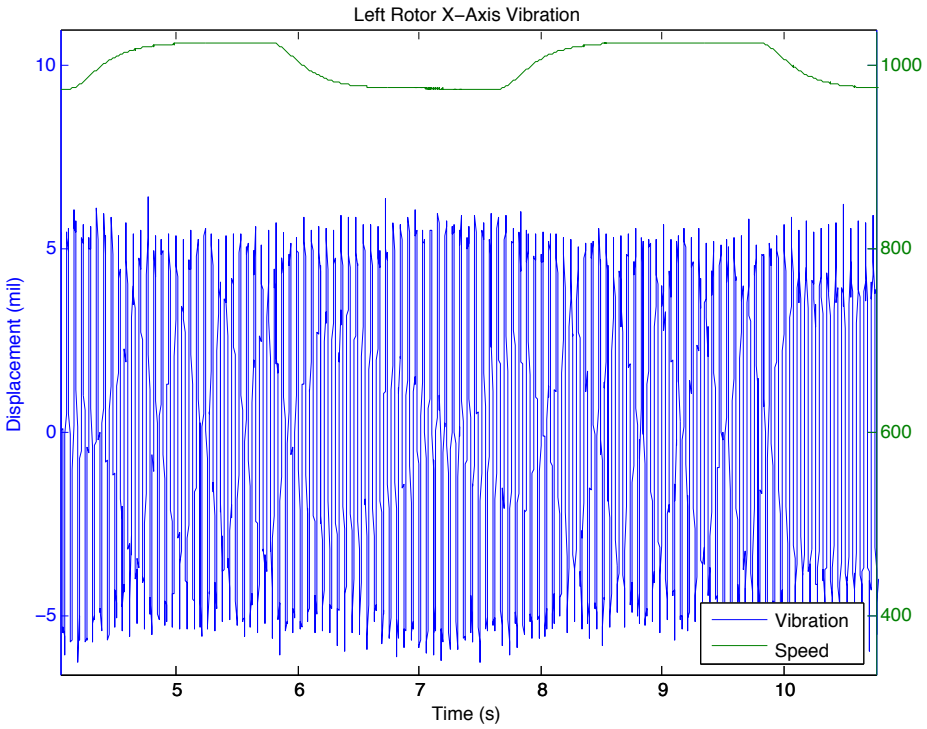

Figure 3.9: Simulated Varying-Speed No-Fault Left Rotor Vibration (Detailed View)

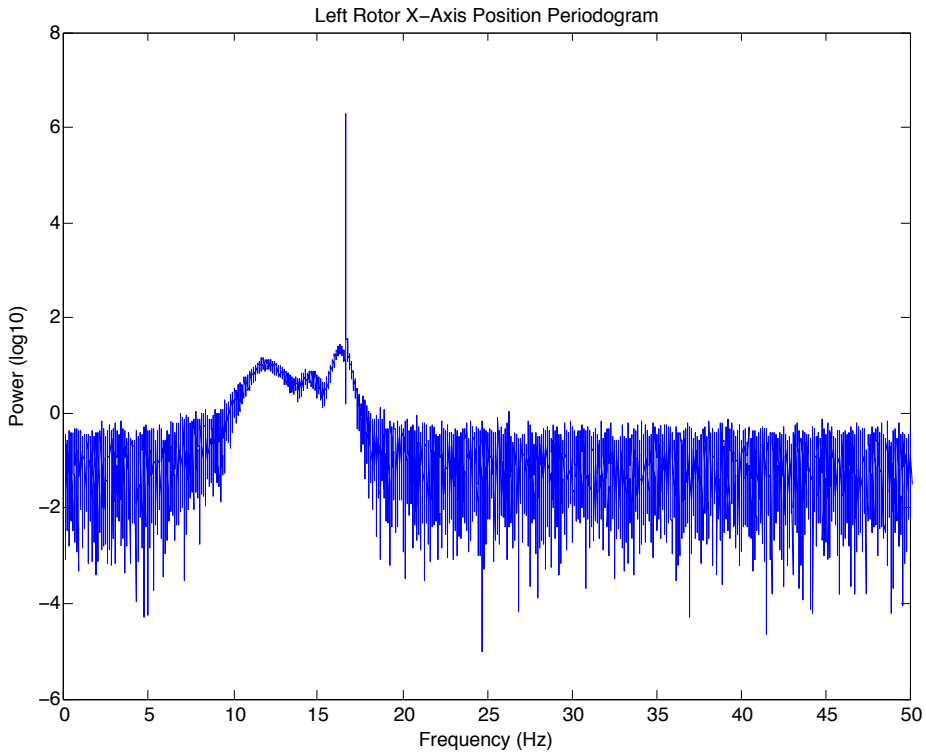

Figure 3.10: Simulated Constant Speed No-Fault Left Rotor Vibration Periodogram

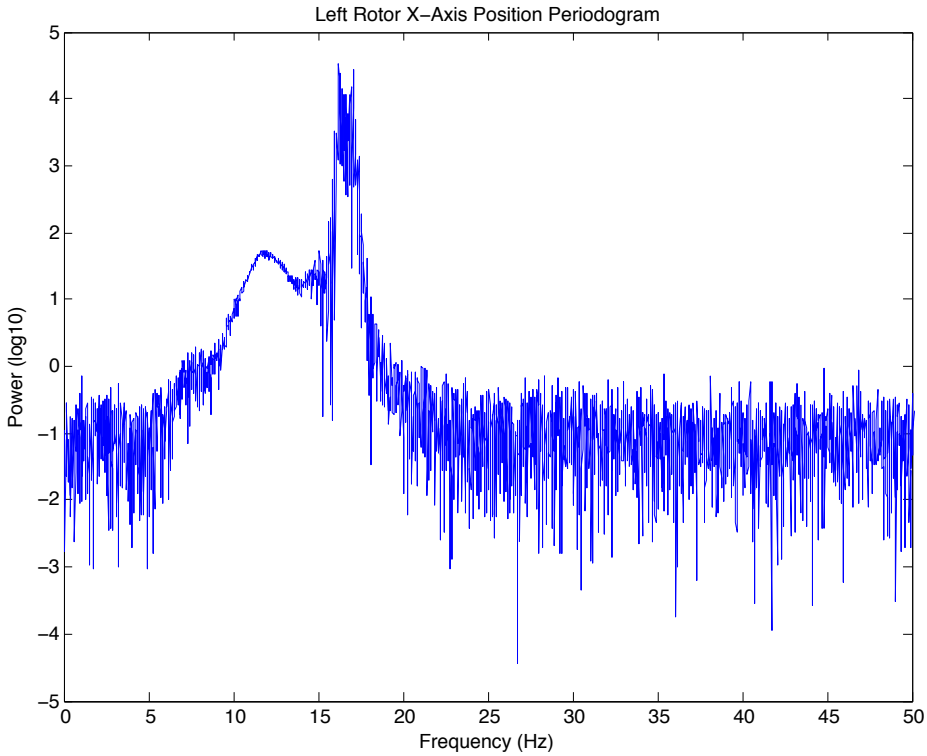

Figure 3.11: Simulated Varying Speed No-Fault Left Rotor Vibration Periodogram

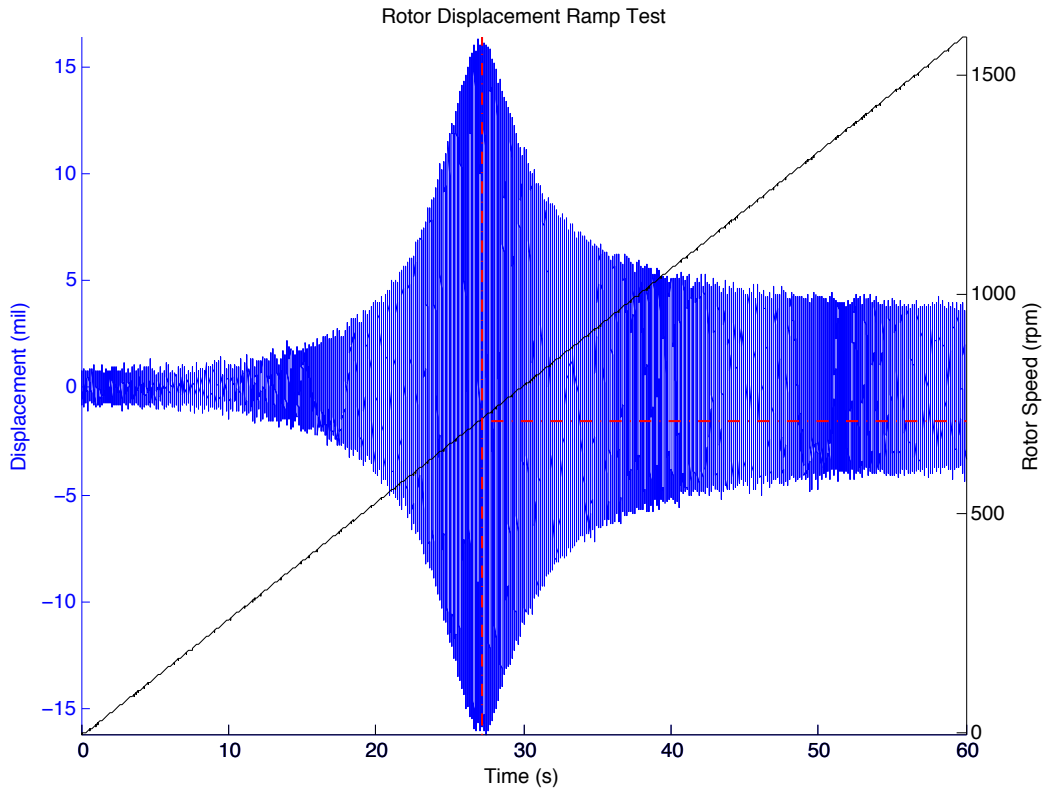

Figure 3.12: Simulated Critical Speed Ramp-Up Test

Table 3.2: Simulated Machine Critical Speeds

Peak	Frequency (RPM)	Frequency (Hz)
1	715	11.92

3.2.2 Critical Speeds

Critical speeds were determined by conducting a ramp-up test on the simulated system. Rotor speed was increased linearly from standstill to 1600 RPM over a period of 60 s, as shown in Figure 3.12. One critical speed was identified within this operating range, which is listed in Table 3.2.

Figure 3.13 plots the X-Y orbit diagrams for the bearings and rotor vibration signals at the first critical speed. The dominance of a 1X component is illustrated by the circular orbits. This critical speed is the product of rotor deflection due to flexibility. Little to no interaction with bearing flexibility is observed, as this would normally manifest as an observable 2X component.

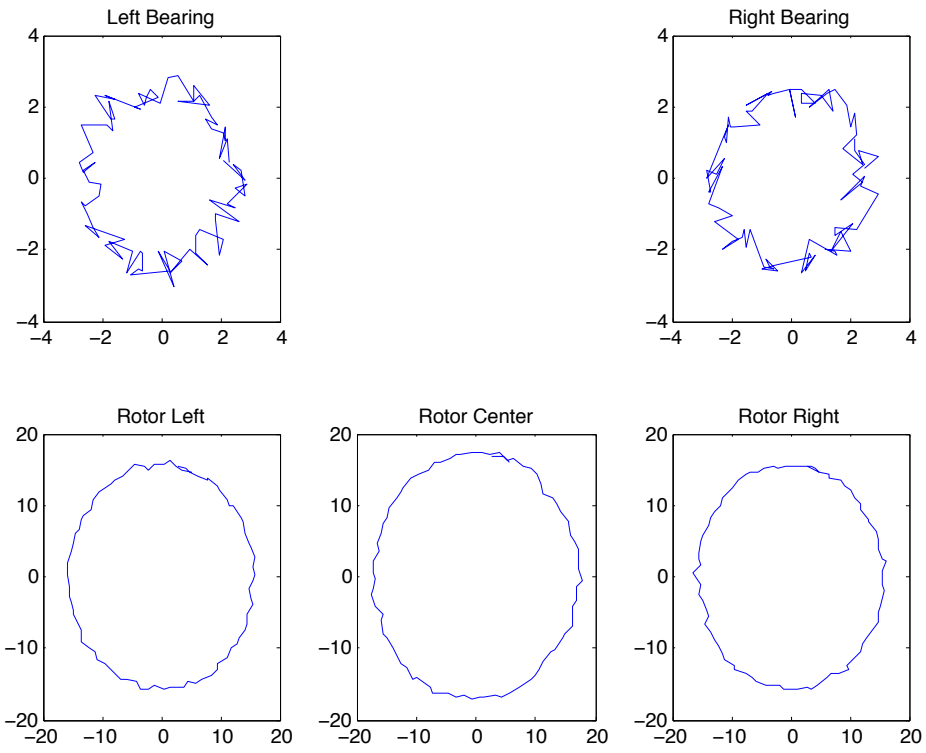

Figure 3.13: Simulated Rotor X-Y Orbit Diagrams (715 RPM)

3.2.3 Operational Deflection Shapes

The behavior of the bearing and flexible rotor simulation can be visualized by plotting the operational deflection shapes (ODS) of the rotor. The simulation was parameterized so that the flexibility subsystem could be selectively disabled. Figure 3.14 shows side and top views of the rotor ODS at a constant 1000 RPM while the flexibility subsystem was disabled. The z-axis position in ODS plots corresponds to shaft position relative to the right end of the rotor, adjacent to the motor. Each line in the figure represents the shape of the rotor at single step in the simulation. These plots show that in the absence of flexibility, the rigid rotor traces a circular orbit around the axial centreline of the machine. The stiffness of the bearings constrains this motion to very small magnitudes.

Figure 3.15 plots the side and top views for the rotor ODS under the same conditions, but with flexibility enabled. The plots show that the ODS is a combination of the rigid-body displacement due to the bearings and the rotor deflection imposed by the flexibility subsystem derived from FEA.

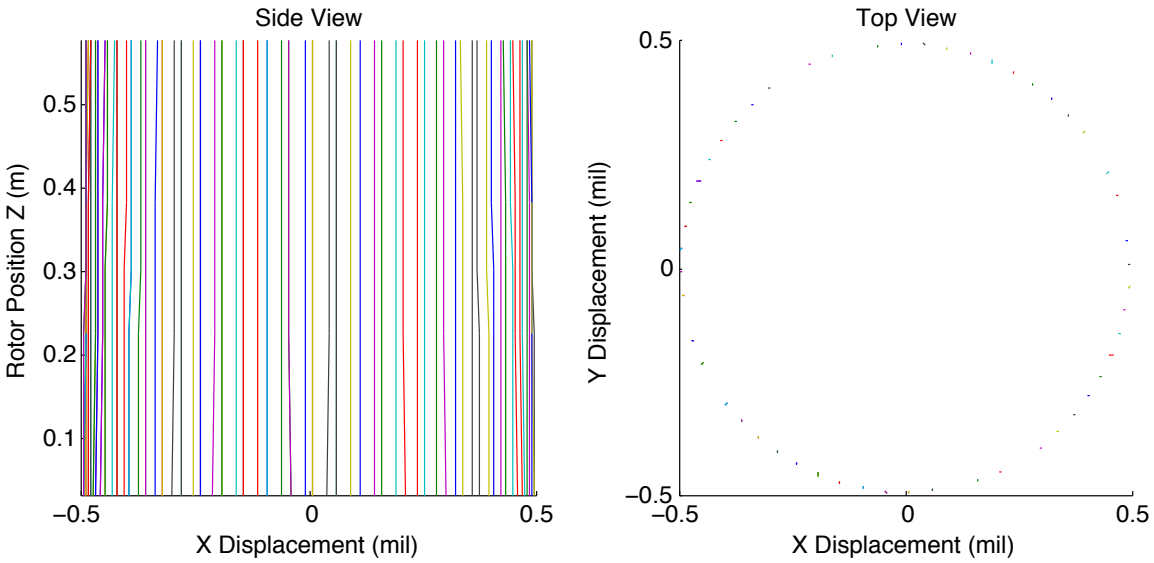

Figure 3.14: Simulated Operational Deflection Shape (No Flexibility)

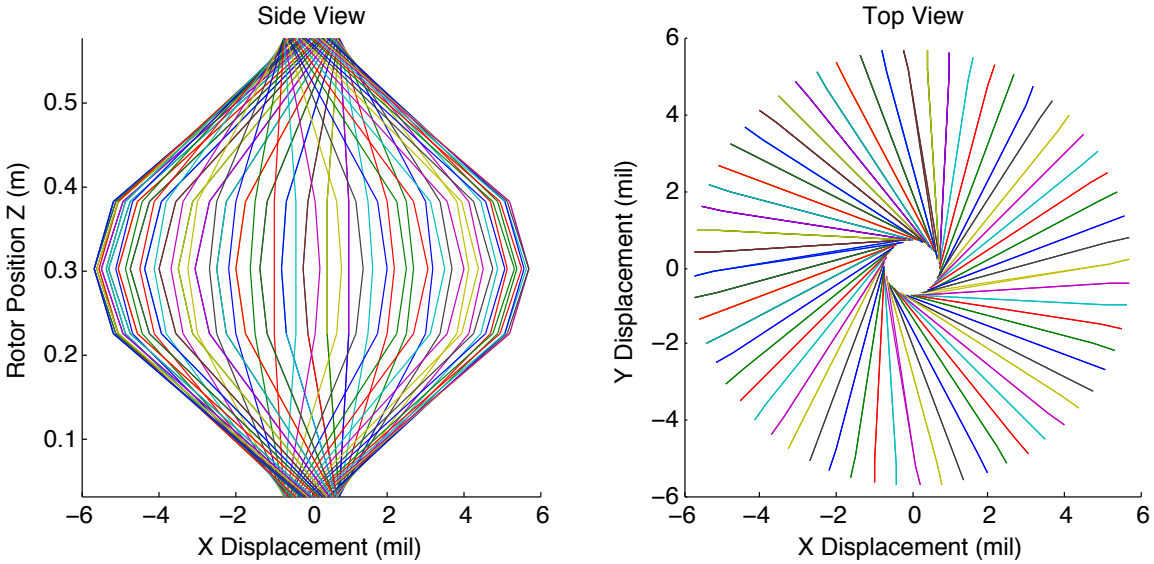

Figure 3.15: Simulated Operational Deflection Shape (Flexibility)

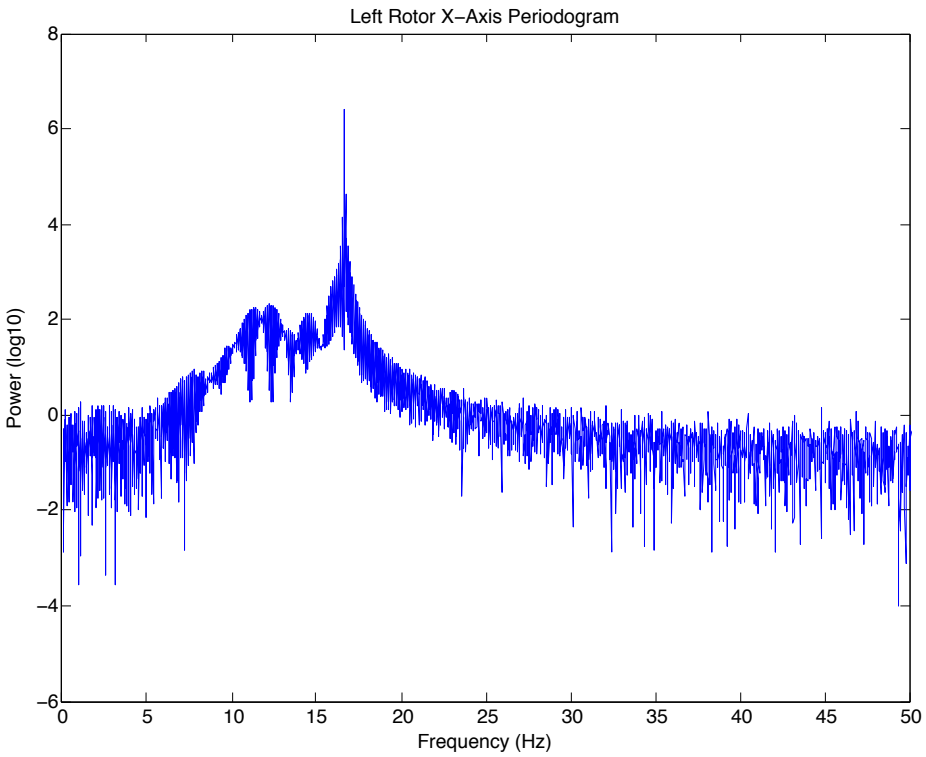

Figure 3.16: Simulated Static Imbalance Left Rotor Vibration Periodogram

3.3 Simulated Machine Faults

Static and dynamic imbalances were induced on the simulated machine. The effect of these faults in the frequency domain is difficult to observe since the spectrum of vibration signals produced by imbalance is concentrated in the 1X frequency and its harmonics. This can be observed in Figures 3.16 and 3.17, which plot periodograms for 6 g static and dynamic imbalance faults induced during constant-speed operation at 1000 RPM. (16.67 Hz) There is little visible difference between these periodograms and the no-fault case plotted in Figure 3.10. The vibration signal power is overwhelmingly concentrated in 1X frequency, and the relative magnitude of that component is comparable across all three periodograms.

Figures 3.18 and 3.19 plots the rotor ODSs for constant-speed operation at 1000 RPM for the 6 g static and dynamic imbalances, respectively. Unlike the periodograms, it is easy to observe the physical effect of the faults on the system. The static imbalance pictured in Figure 3.18 resulted in an increase of approximately four times in the peak ODS magnitude, although the shape is similar to that created by the residual imbalance in the no-fault system shown in Figure 3.15. The dynamic imbalance picture in Figure 3.19 creates a significant change in the ODS, with greater deflection at the left bearing position than at the right

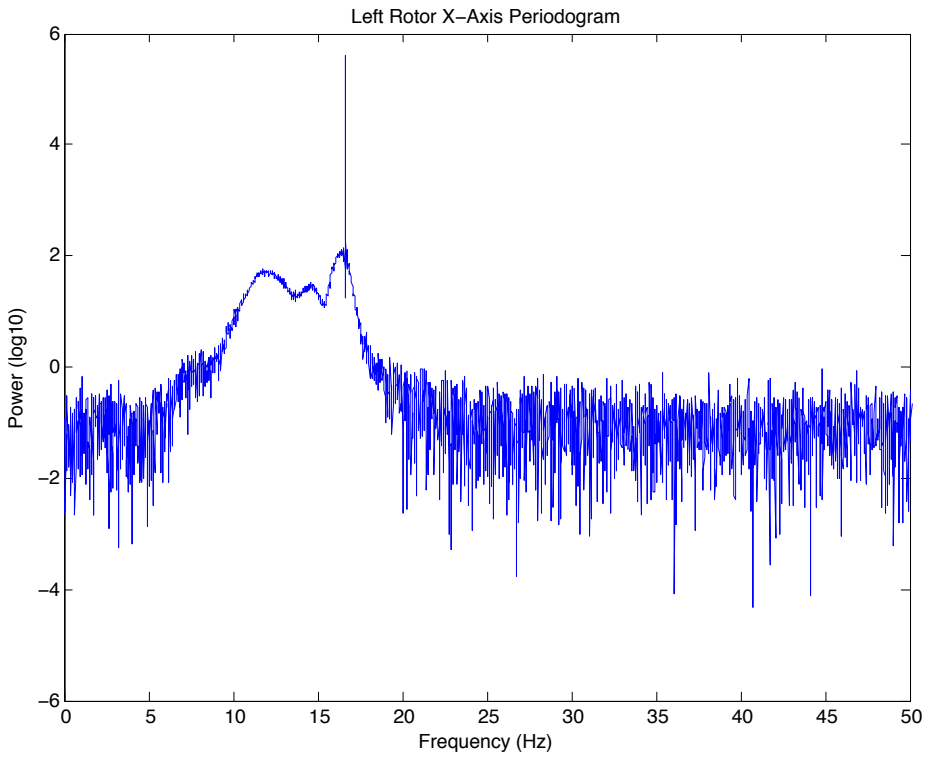

Figure 3.17: Simulated Dynamic Imbalance Left Rotor Vibration Periodogram

bearing. The peak deflection is comparable to the no-fault case, however.

These figures illustrate the challenge in detecting imbalance faults. The physical influence of the faults is clear, but difficult to discern when restricted to observation of vibration spectrum or magnitude. The goal of the subspace fault detection method presented in subsequent sections is to take advantage of the physical effects of vibration illustrated by Figures 3.18 and 3.19 to detect these faults.

3.4 Physical Machine Overview

A laboratory apparatus based on the simulated machine design previously described was constructed using a combination of off-the-shelf and custom-machined parts. A photograph of the physical machine is provided in Figure 3.20. The rotating components were based on a steel shaft, coupled to a 24 V DC motor via a flexible coupling. The shaft is supported by two sleeve bushings mounted on machined aluminum supports and bolted to a heavy aluminum base atop a lab bench. Vibration was measured by two-axis accelerometers mounted on the bearing supports, and by inductive proximity sensors mounted on aluminum brackets over the shaft at points between the center and outer flywheels. The rotor speed is governed by an

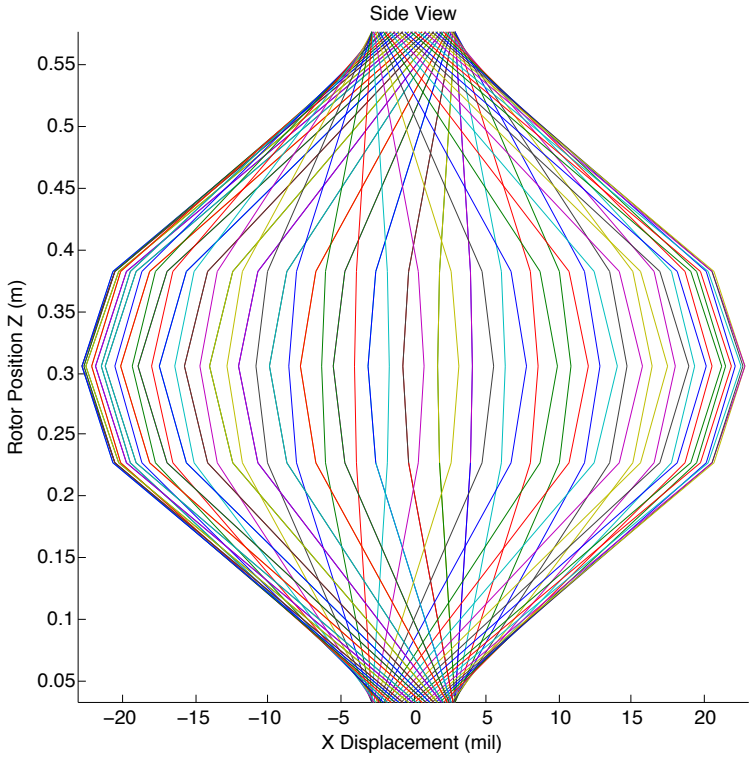

Figure 3.18: Simulated Static Imbalance Operational Deflection Shape

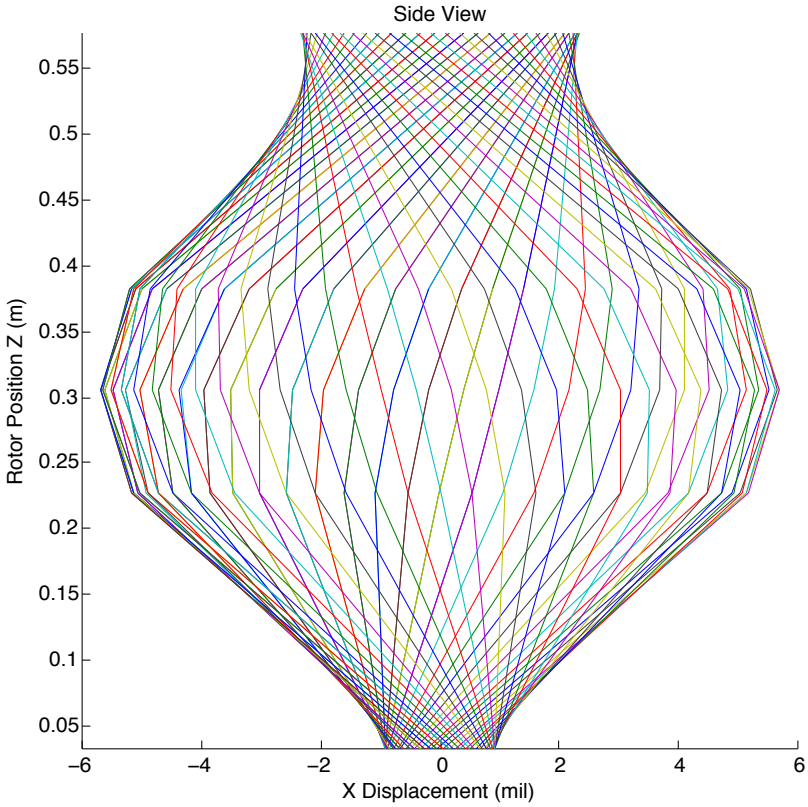

Figure 3.19: Simulated Dynamic Imbalance Operational Deflection Shape

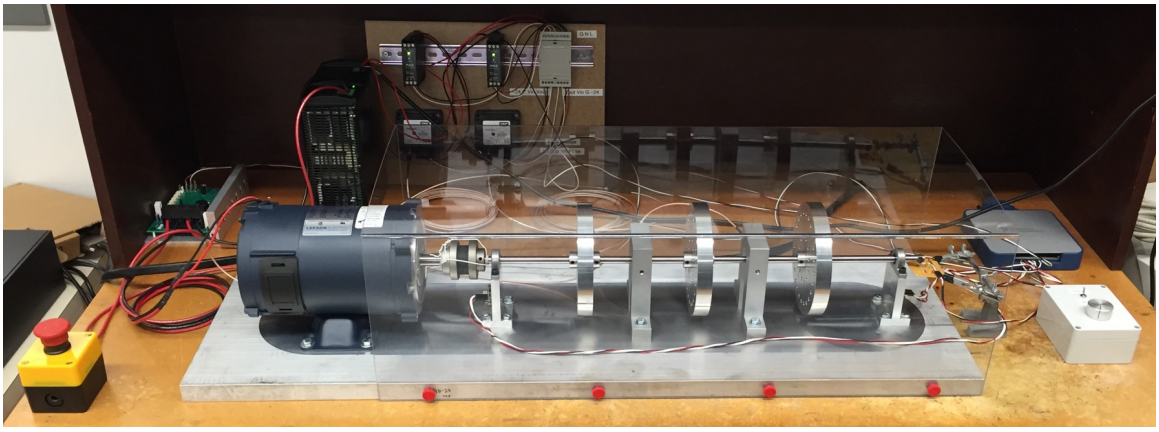

Figure 3.20: Physical Machine

off-the-shelf DC speed controller and a magnetic speed sensor. Rotor speed was determined using a Schmitt-trigger magnetic sensor to detect the alternating north and south poles of neodymium magnets attached to the end of the shaft. The system was controlled by a PC running MATLAB, using a National Instruments data acquisition card (DAQ) to interface with the sensors and speed controller.

Each flywheel mounted on the physical machine had the same pattern of concentric rings of holes drilled at intervals around the hub as on the simulated machine. Controlled imbalances were created by attaching bolts through these holes and securing them with nuts. Each nut and bolt assembly weighed 10 g, so this is the smallest imbalance possible. To provide a reference point, the outer flywheel holes in line with the setscrews holding the flywheel on the rotor were selected as the 0° position. Static imbalances were created by attaching a bolt at this point on the center flywheel. Dynamic imbalances were created by attaching one bolt at the 0° position on the right flywheel and 180° on the left flywheel.

Vibration was originally measured using only the accelerometers mounted on the bearing supports, but these sensors were found to have limited sensitivity to rotor vibration and the signal-to-noise ratio was very poor, as is often the case for machines with flexible rotors and a heavy support structure. As a result, inductive proximity sensors were added and eventually used as the sole source of vibration data. These inductive eddy probes, manufactured by SKF to the API 670 standard, measured the distance of the surface of a conductive object from the probe tip over a range of 80 mil. (2 mm) As per API 670, the output of the sensor driver is a negative voltage proportional to the distance of the object from the tip, decreasing from 0 to -24 V as the object becomes more distant. Signal conditioners were used to convert the voltage range to the ±10 V range accepted by the DAQ. Analog signals

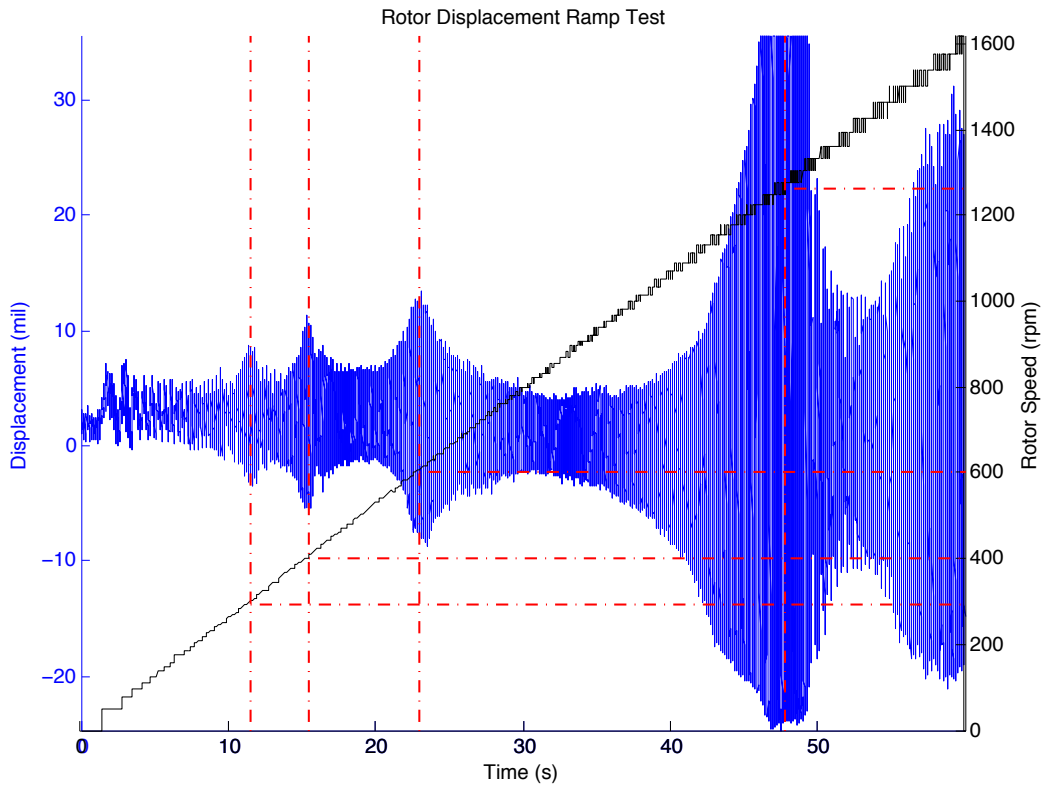

Figure 3.21: Physical Machine Critical Speed Ramp-Up Test

measured by the DAQ were oversampled at a rate of 10 kHz, and then the measured signals were reduced to 1 kHz in MATLAB using the built-in decimation function. This function automatically applied a low-pass filter to the measured signal prior to decimation.

3.5 Physical Machine Vibration Analysis

3.5.1 Critical Speeds

Critical speeds were obtained for the physical machine by conducting a ramp-up test from standstill to 1600 RPM over a period of 60 s, as shown in Figure 3.21. As can be observed from this figure, the behavior of the physical machine was considerably more complicated than the simulated machine. Four critical speeds were observed within the possible operating range, which are listed in Table 3.3.

Vibration magnitude was most pronounced at the third and fourth critical speeds. The machine was normally operated at a constant speed of 1000 RPM, a supercritical speed located at a vibrational minimum. The machine was never operated at or above the fourth critical speed, as resonance became extremely severe and rotor displacement began to exceed the sensor limits.

Table 3.3: Physical Machine Critical Speeds

Peak	Frequency (RPM)	Frequency (Hz)
1	295	4.917
2	400	6.667
3	600	10.00
4	1265	21.08

3.5.2 Physical Machine Faults

Unlike the simulated machine, it was not possible to plot the rotor ODS for the physical machine as the instrumentation was only capable of measuring rotor position for two degrees of freedom, due to the expense of additional proximity sensors. Both proximity sensors could be mounted at a single location, allowing simultaneous measurement in both axes so that X-Y orbit diagrams could be plotted for the rotor at that point. Figure 3.22 shows the rotor orbit diagram from the left sensor position for a 2.5 s selection of three constant-speed tests at 1000 RPM. The orbits for a no-fault test, an inner 10 g static imbalance, and an outer 10 g dynamic imbalance were plotted on the same figure for comparison.

The orbit diagram illustrates the effect of faults on the physical machine. The no-fault system traced an approximate circle, as the motion was dominated by deflection of the rotor associated with the 1X component. The motion was not perfectly circular, indicating the presence of harmonics or other factors that were not accounted for, such as bearing nonlinearities. The introduction of a static imbalance increased the overall magnitude of the orbit as expected, and the greater contribution of the 1X diminished the relative importance of the unaccounted factors. In contrast, the dynamic imbalance reduced the magnitude of vibration at the measurement point. Harmonics and other effects appeared to play a larger role in this case.

Figure 3.23 provides another comparison of the no-fault system and the two faults in the frequency domain. This figure superimposes the periodograms for each case into a single plot. There was very little to distinguish the three cases by their spectral content. The static imbalance was identified with a proportionally larger contribution from the 1X component, but otherwise its higher-frequency spectrum was undifferentiated. The no-fault and dynamic imbalance spectrums were nearly identical.

An unaccounted peak was observed near 20 Hz in each of the physical machine periodograms. This peak was present in all three cases, with little difference in magnitude or frequency regardless of the fault status. This effect was not present in the simulated ma-

chine, and was not anticipated by any aspect of the design. This contribution may explain the non-circularity of the rotor orbits in Figure 3.23. As Figure 3.21 also demonstrated, the physical machine was not a perfect realization of the idealized machine that was used in the simulations. These differences show the challenge posed by applying the subspace fault detection method to a practical machine that is only approximated by the model obtained from analysis and simulation.

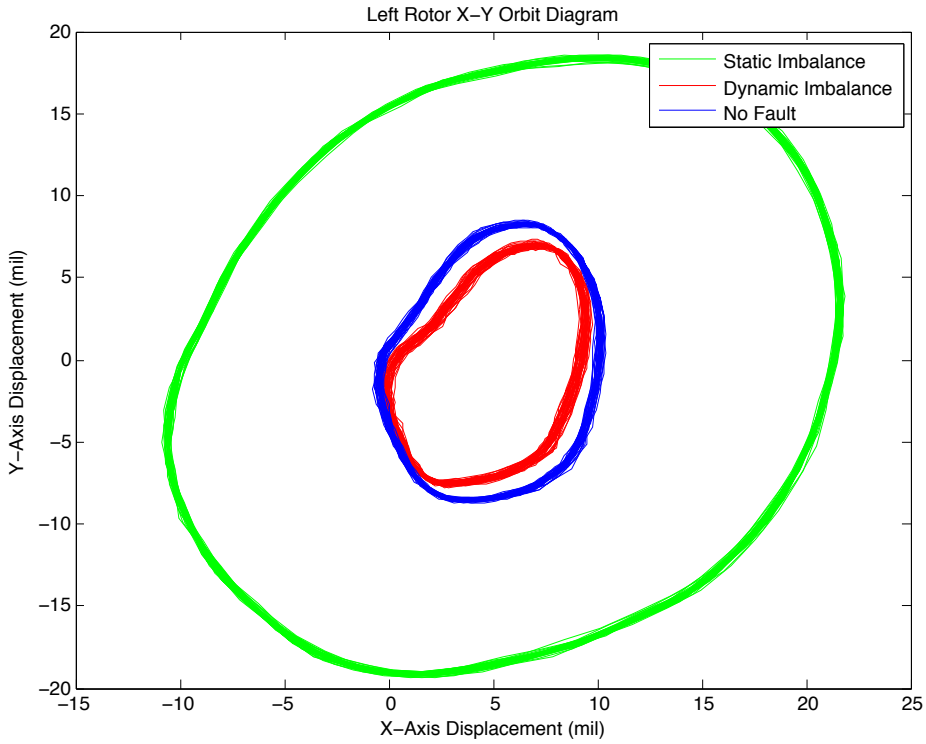

Figure 3.22: Physical Machine Left Rotor Orbit Diagrams

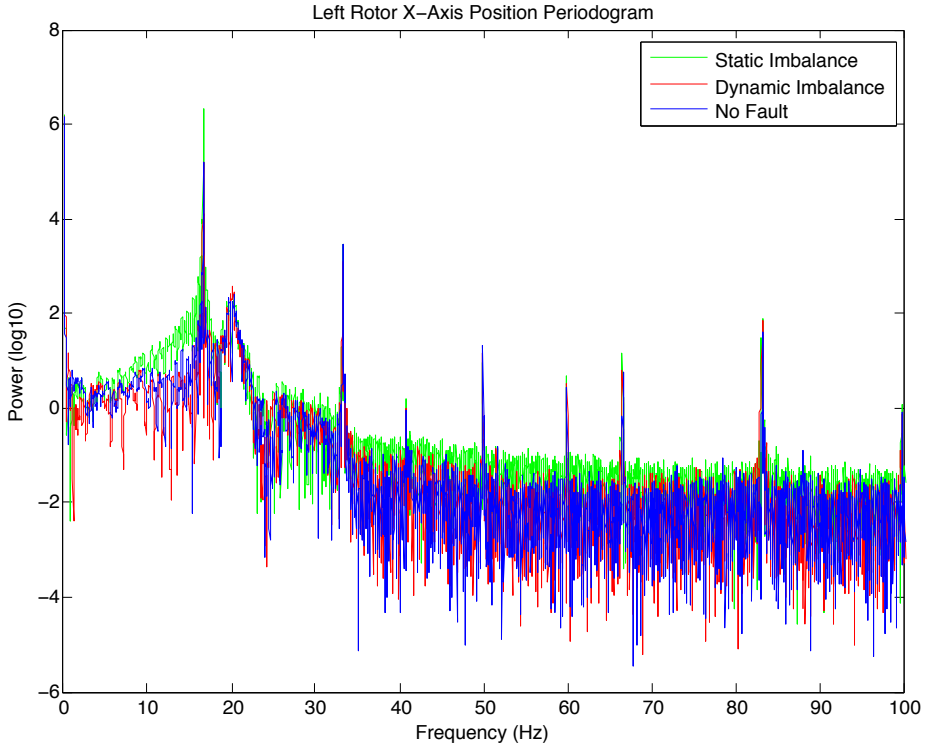

Figure 3.23: Physical Machine Left Rotor Vibration Periodograms

Chapter 4

Subspace Imbalance Fault Detection

4.1 Methodology

The vibration-based fault detection algorithm implemented for this thesis was derived from the subspace method described by Basseville et al [18]. This method uses an asymptotic local approach fault detection scheme by applying subspace methods to a no-fault modal model and output data covariance matrices. A brief overview of the subspace method is presented in this section, followed by sample calculations for the simulated machine.

The asymptotic local approach consists of transforming the fault detection problem into a statistical test between two hypothesis: H_0, the no-fault hypothesis, and H_1, the hypothesis that a fault has occurred. A local approach algorithm produces a residual whose distribution is statistically Gaussian with constant covariance for faults that correspond to small changes in system parameters. The residual has a zero-mean distribution when H_0 holds, and a non-zero mean when H_1 holds:

$$\begin{aligned} H_0 &: \zeta_n(\theta_0) \rightarrow \mathcal{N}(0, \Sigma(\theta_0)) \\ H_1 &: \zeta_n(\theta_0) \rightarrow \mathcal{N}(M(\theta_0)\Upsilon, \Sigma(\theta_0)) \end{aligned} \tag{4.1}$$

where ζ_n is the residual vector, θ_0 is a parameter representing the no-fault system model, $M(\theta_0)$ is the mean residual sensitivity matrix, a Jacobian matrix derived from θ, and $\Sigma(\theta_0)$ is the residual covariance matrix. Υ is an unknown fault vector that corresponds to the specific residual. The residual matrices are constant and may be precomputed from the no-fault model or derived from sample data.

Evaluation of the residual then becomes a question of determining whether it is significantly different from zero. This is usually accomplished with a χ^2 test. The residual vector

is first normalized to unit variance, then reduced to a scalar test statistic that has a χ^2 distribution if no fault has occurred. The test statistic is compared with a threshold value to determine if a fault has occurred. The threshold is chosen to give the desired level of confidence that when the test statistic exceeds the threshold a fault is the cause, rather than random variation. The core of the fault detection algorithm lies in generating the residual vector from the no-fault model and measured output data.

The algorithm assumes that the machine can be accurately modeled using a linear, time-invariant, stochastic, discrete-time state-space model with additive Gaussian state and measurement noise:

$$\begin{aligned} X_{k+1} &= FX_k + \epsilon_k \\ Y_k &= HX_k + \upsilon_k \end{aligned} \tag{4.2}$$

This model is sufficient for capturing the vibration dynamics of a rotor operating at a constant rotational speed. However, a full state-space realization is not required to implement the algorithm. Instead, the system can be modeled entirely in terms of its modal structure. For convenience of calculation, the eigenvalues and eigenvectors are grouped into a column vector known as the system parameter θ:

$$\theta = \begin{bmatrix} \Lambda \\ vec\Phi \end{bmatrix} \tag{4.3}$$

where Λ is a vector of the system eigenvalues λ, Φ is a matrix of the observed eigenvectors, (the product of the output matrix H and the eigenvector matrix) and *vec* is the vector stacking operator whose output is a column vector consisting of the columns of Φ stacked in order.

Small changes to the modal structure can be characterized as the addition of an unknown, but fixed fault vector Υ to the system parameter θ. It is this representation of the fault as a small change in the system parameter that is the essence of the local approach. The hypotheses H_0 and H_1 are formally defined in terms of the system parameter as follows:

$$\begin{aligned} H_0 &: \theta = \theta_0 \\ H_1 &: \theta = \theta_0 + \Upsilon/\sqrt{n} \end{aligned} \tag{4.4}$$

where n is the number of data samples and Υ is the unknown fault vector.

The task of the algorithm is then to generate a residual with known statistical distributions that can be tested to distinguish between hypotheses H_0 and H_1. The residual can be

generated from output data in real time, but the calculation requires several intermediate results that must be computed ahead of time from the no-fault model.

An extended observability matrix using a modal coordinate basis can be defined in terms of the eigenvalues and eigenvectors of the no-fault system model:

$$\mathcal{O}_{p+1}(\theta) = \begin{bmatrix} \Phi \\ \Phi\Delta \\ \vdots \\ \Phi\Delta^p \end{bmatrix} \tag{4.5}$$

where Δ is a diagonal matrix of the eigenvalues, Φ is the observed eigenvector matrix, and p is an integer that is at least as large as the true system order. A larger value for p will result in a longer residual vector and more calculations to generate each residual.

Measured output data is incorporated into the residual by calculating a block-Hankel matrix of the output covariances:

$$\mathcal{H}_{p+1,q} = \begin{bmatrix} R_{\tau+1} & R_{\tau+2} & \cdots & R_{\tau+q} \\ R_{\tau+2} & R_{\tau+3} & \cdots & R_{\tau+q+1} \\ \vdots & \vdots & \ddots & \vdots \\ R_{\tau+p+1} & \cdots & \cdots & R_{\tau+p+q} \end{bmatrix} \tag{4.6}$$

where $R_j = E(Y_{k+j}Y_k^T)$ is the covariance of the measured output data at lag time j, τ is the measurement noise correlation, taken as zero, and $q \geq p+1$. Each R_j is an $r \times r$ submatrix if the system is multi-output. The integer q is selected to ensure that the rank of $\mathcal{H}$ is not constrained by column width. A larger value may be used, but it will increase the length of the residual vector and the number of calculations required to generate it.

The justification for this fault detection algorithm is the observation that $\mathcal{O}_{p+1}(\theta_0)$ and $\mathcal{H}_{p+1,q}$ have the same left kernel space if the no-fault hypothesis H_0 holds. If this is the case, it is possible to generate a Gaussian residual vector that has a zero-mean distribution. The residual calculation requires a matrix S of nullity m whose columns form an orthonormal basis of the left kernel space of $\mathcal{O}_{p+1}(\theta_0)$. The S matrix is obtained by a SVD of $\mathcal{O}_{p+1}(\theta_0)$.

The following property holds for S and $\mathcal{H}_{p+1,q}$ when calculated from the no-fault system:

$$S^T(\theta_0)\mathcal{H}_{p+1,q} = 0 \tag{4.7}$$

The residual vector calculation follows an analogous formulation:

$$\zeta_n(\theta_0) = \sqrt{n}\ vec(S^T(\theta_0)\mathcal{H}_{p+1,q}) \tag{4.8}$$

where n is the number of data samples used in the calculation of $\mathcal{H}$. In Equation 4.7 the matrix $\mathcal{H}$ provides information on the state of the actual system, which may or may not

be faulty, while S represents the no-fault system model. $\zeta_n(\theta_0)$ is a column vector whose length is given by $q[(p+1)r - m]$.

Once the evaluation problem has been reduced to determining whether the residual represents a Gaussian distribution with non-zero mean, there is a wide array of standard statistical tools that can be applied to create a decision function. Basseville suggests a form of the χ^2 test based on empirical residual sensitivity Jacobian and covariance matrices pre-calculated from the no-fault system [21]. For the purposes of this thesis a simplified version of the χ^2 test based on a norm-squared test statistic was used to evaluate the residuals, as described in the following section.

4.2 Residual Evaluation

The residual produced by the subspace fault detection method is a Gaussian-distributed vector where the mean of the distribution is non-zero if and only if a fault has occurred. The variance of the distribution is not affected by a fault. The evaluation of a single-valued residual is a simple problem, typically performed by comparing the residual with a threshold value obtained from a standardized χ^2 distribution table after normalizing the residual to unit variance. If the residual exceeds the threshold for a given confidence level, often 95% or 99.5%, a fault has occurred.

Evaluating a vector-valued residual is somewhat more involved. There are several possible methods: testing each component of the vector individually, testing the joint probability density function of the vector, or testing the norm-squared of the residual vector. This thesis applies the latter technique, as described by Chowdhury in [30]. It can be shown that if the no-fault residual $\zeta_n(\theta_0)$ is Gaussian with zero mean and non-unit variance, a test statistic r_{norm} can be derived that is χ^2 distributed with $k-1$ degrees of freedom, if k is the length of the residual vector $\zeta_n^t(\theta_0)$:

$$r_{norm} = \zeta_n^t(\theta_0) Q^{-1} \zeta_n(\theta_0) \tag{4.9}$$

where Q is the covariance matrix of the residual vector. Q is necessary to normalize the variance of the residual vector. It was shown by Chowdhury that this norm-squared method is theoretically equivalent to evaluation of the joint PDF, but more convenient to compute in an online fault detection system. The test statistic r_{norm} may be computed in various ways, depending on the choice of normalization technique for the residual vectors. If the individual components of the residual are independent random variables, it is possible to normalize each component individually by dividing it by the square root of the variance of

that component, rather than calculating Q^{-1}. The residuals calculated for this thesis were calculated by normalizing individual components. The variance vector was obtained by simulating the no-fault system for five minutes, calculating residual vectors, and computing the sample variance of each residual component across the entire simulation results.

r_{norm} is a scalar that can be compared with a threshold value T_r to determine if the no-fault hypothesis H_0 should be rejected. If r_{norm} exceeds T_r, a fault is judged to have occurred. The specific value of T_r is selected from a table of χ^2 values indexed by the required degrees of freedom and confidence level. The test statistic for the second-order, two-output fault detection system has 23 degrees of freedom. A confidence level of 95% was used. For these choices the χ^2 table provides a threshold T_r of 35.17.

4.3 Sample Calculations

This section demonstrates the calculations required to generate and evaluate a residual vector based on the no-fault model established in the previous chapter and sample data obtained from simulation. The first step was to establish a modal structure model for the no-fault system. A second-order model was used, with two measured outputs: x-axis rotor position at the left and right rotor position sensors.

The natural frequencies and mode shapes of the machine were derived in the machine modeling chapter. The subspace method required eigenvalues in complex-conjugate pairs. A pair of continuous-time eigenvalues were calculated from the natural frequency of 11.92 Hz using a damping ratio of 0.05, then converted to discrete time to obtain the following eigenvalue vector:

$$\Lambda = \begin{bmatrix} 0.9935 + 0.0745i \\ 0.9935 - 0.0745i \end{bmatrix} \tag{4.10}$$

The corresponding observed eigenvector matrix was assembled from the mode shapes at the rotor measurement points, listed in the left and right rotor columns in Table 3.1:

$$\Phi = \begin{bmatrix} -2.3513 & -2.3513 \\ -2.3513 & -2.3513 \end{bmatrix} \tag{4.11}$$

The no-fault system parameter was assembled by stacking the eigenvalues and the product of the output matrix and the eigenvector matrix according to Equation 4.3:

$$\theta = \begin{bmatrix} \Lambda \\ vec\Phi \end{bmatrix} = \begin{bmatrix} 0.9935 + 0.0745i \\ 0.9935 - 0.0745i \\ -2.3513 \\ -2.3513 \\ -2.3513 \\ -2.3513 \end{bmatrix} \tag{4.12}$$

Equation 4.12 represents a complete model of the vibration dynamics of the no-fault system. The next step was to obtain an extended observability matrix from the modal model, as in Equation 4.5. The dimension of the observability matrix, p, is an integer that must be at least as large as the true system order. A system order of $p = 2$ was used. This gave the following result:

$$\mathcal{O}_3(\theta) = \begin{bmatrix} \Phi \\ \Phi\Delta \\ \Phi\Delta^2 \end{bmatrix} = \begin{bmatrix} -2.35 + 0.00i & -2.35 + 0.00i \\ -2.35 + 0.00i & -2.35 + 0.00i \\ -2.34 - 0.18i & -2.34 + 0.18i \\ -2.34 - 0.18i & -2.34 + 0.18i \\ -2.31 - 0.35i & -2.31 + 0.35i \\ -2.31 - 0.35i & -2.31 + 0.35i \end{bmatrix} \tag{4.13}$$

The subspace method requires a set of orthonormal basis vectors for the left kernel space of the extended observability matrix in Equation 4.13. This is the key input that encapsulates the no-fault model in the residual generation algorithm. This is known as the S matrix, and it could be obtained in a straightforward fashion applying the built-in *null* function in MATLAB to the transpose of the observability matrix:

$$S = \begin{bmatrix} -0.35 + 0.09i & -0.35 + 0.09i & -0.20 + 0.35i & -0.20 + 0.35i \\ -0.03 - 0.10i & -0.03 - 0.10i & 0.34 - 0.41i & 0.34 - 0.41i \\ 0.88 + 0.01i & -0.12 + 0.01i & -0.14 + 0.06i & -0.14 + 0.06i \\ -0.12 + 0.01i & 0.88 + 0.01i & -0.14 + 0.06i & -0.14 + 0.06i \\ -0.19 - 0.01i & -0.19 - 0.01i & 0.57 - 0.03i & -0.43 - 0.03i \\ -0.19 - 0.01i & -0.19 - 0.01i & -0.43 - 0.03i & 0.57 - 0.03i \end{bmatrix} \tag{4.14}$$

The matrix given in Equation 4.14 must be calculated before the fault detection algorithm is applied online. When the method is applied online, measurement data is collected from the sensors and stored in the measured data matrix Y, where each row is a sample and each column represents a sensor. A residual vector can be generated for the entire data matrix, but in practice it is applied to a selection of samples from a smaller window. All results quoted in this thesis used a 1 s window.

Using the selection of rows from the data matrix corresponding to the current window, the next step was to assemble the block-Hankel matrix from Equation 4.6. First, the covariance matrices R_j were calculated for each of the required time lag values j from 1 to $p + q$. The block-Hankel matrix was assembled from these covariance matrices. This matrix depends on the particular sample data used in its construction, but for illustration the block-Hankel matrix assembled for the 30 s window of a no-fault simulation is included

below:

$$\mathcal{H}_{30s} = \begin{bmatrix} 13.50 & 13.40 & 13.27 & 13.17 & 12.91 & 12.80 \\ 13.41 & 13.31 & 13.20 & 13.10 & 12.85 & 12.74 \\ 13.27 & 13.17 & 12.91 & 12.80 & 12.40 & 12.29 \\ 13.20 & 13.10 & 12.85 & 12.74 & 12.35 & 12.24 \\ 12.91 & 12.80 & 12.40 & 12.29 & 11.76 & 11.64 \\ 12.85 & 12.74 & 12.35 & 12.24 & 11.72 & 11.60 \end{bmatrix} \tag{4.15}$$

The residual vector for this window was calculated by taking the product of S and $\mathcal{H}_{30s}$, according to the formula provided in Equation 4.8. The result was a complex-valued 24-element residual vector, where each element was a random variable with Gaussian distribution:

$$\zeta_n(\theta_0) = \begin{bmatrix} 1.50 - 0.29i \\ -0.63 - 0.29i \\ -0.10 - 1.17i \\ -2.03 - 1.17i \\ 1.49 - 0.30i \\ -0.79 - 0.30i \\ -0.12 - 1.20i \\ -2.02 - 1.20i \\ 1.49 - 0.23i \\ -0.44 - 0.23i \\ -0.10 - 0.94i \\ -1.70 - 0.94i \\ \vdots \end{bmatrix} \begin{bmatrix} \vdots \\ 1.54 - 0.25i \\ -0.37 - 0.25i \\ -0.17 - 1.01i \\ -1.77 - 1.01i \\ 1.35 - 0.21i \\ -0.26 - 0.21i \\ -0.27 - 0.86i \\ -1.41 - 0.86i \\ 1.37 - 0.21i \\ -0.23 - 0.21i \\ -0.25 - 0.85i \\ -1.44 - 0.85i \end{bmatrix} \tag{4.16}$$

The final step was to reduce the residual vector to a scalar test statistic. First, the vector was normalized to unit variance by dividing each element by the square root of the variance for that element. The latter was a vector of variances for each element, precalculated from no-fault data as described in the previous section. The norm-square of the normalized vector was calculated as follows, giving the test statistic for the 30 s window. As expected, the test statistic was below the detection threshold.

$$r_{norm} = \zeta_n^t(\theta_0)\zeta_n(\theta_0) = 5.63 < T_r = 35.17 \tag{4.17}$$

Chapter 5

Experimental Results

5.1 Overview

This chapter presents results for the subspace fault detection method previously described, and for comparison two alternative schemes that have received attention in recent years: sinusoidal synthesis (SS) and the Hilbert-Huang Transform. (HHT) Each method represents a distinct approach to the same problem of detection rotating machine faults.

The subspace method is a model-based time-domain algorithm that detects small changes in the modal structure of a vibrating system. It requires no manual intervention beyond the initial setup of determining the no-fault system model and choosing a detection threshold. It is well-suited to implementation as an automatic real-time condition monitoring system. It is deliberately insensitive to transient effects like noise or impulsive faults, such as those caused by gear or rotor cracking.

SS is a time-series method that is similar to the AR matched-model prediction error signal method. The particular version used for this thesis eliminates the need for a predetermined model by using frequency estimators to adapt a sum-of-sinusoids model to the vibration signal during operation. This algorithm is particularly effective at detecting transient impulsive faults, such as those produced by gear cracks, and is well-suited to implementation as an automatic condition monitoring system. However, it is less effective at detecting non-transient faults as it tends to adapt to slower-scale changes in the underlying system.

Unlike the other two methods, the HHT operates in the frequency domain and requires subjective human interpretation of the results. It is not suitable for automatic condition monitoring, but it is still useful for demonstrating the difficulty of detecting imbalance faults with even the most modern frequency-domain techniques. The HHT consists of an empirical mode decomposition (EMD) of the vibration signal into a set of intrinsic mode functions,

(IMFs) followed by Hilbert transformation of the IMFs. The results can be plotted to illustrate the spectral content of the vibration signal as a function of time. It is often possible to infer the presence of a fault from characteristic patterns in the time-frequency plot.

5.2 Simulated Machine Fault Detection

5.2.1 Signal Characteristics

The three fault detection algorithms were applied to data collected from the simulated rotor imbalance machine for static and dynamic imbalance faults of 2 g, 4 g, 6 g, and 8 g. The machine was operated at a constant 1000 RPM for all tests, and configured with a residual 2 g imbalance on the center flywheel. The simulation was parameterized so that controlled static and dynamic imbalances could be induced at any time during the simulation through a Variable Mass SimMechanics block. Imbalances were created at the 30 s point in each 60 s simulation.

Figure 5.1 shows several periods of the four vibration signals, x- and y-axis rotor position signals from both left and right sensor positions, starting at the 10 s mark for a no-fault simulation. While four signals were available, fewer were actually used in any given algorithm. The subspace method made use of the x-axis position signal at both sensor locations, while the SS and HHT methods used only the x-axis left rotor position signal.

Figures 5.2 and 5.3 illustrate the effect of a pronounced fault on the four vibration signals. Figure 5.2 shows the effect of a 6 g static imbalance introduced at the 30 s mark. An immediate and significant increase in magnitude was observed in all four signals. Transient effects were also noted immediately after the fault is introduced. Figure 5.3 shows the same measurements taken for a 6 g dynamic imbalance introduced at the 30 s mark. In contrast to the previous example, it was difficult to observe any effect on the vibration signals even though this fault represents a severe imbalance. In addition, no transient effects were discernible near the fault. While many techniques may be appropriate to detect a static imbalances given the obvious nature of their effect on vibration signals, detecting a fault that is not apparent to human analysis presents a greater challenge.

5.2.2 Subspace Method

Using the machine model and the intermediate calculations described in the previous chapter, residual vectors were calculated for 1 s windows at corresponding intervals throughout each simulation using the x-axis rotor position signals at the left and right sensor positions.

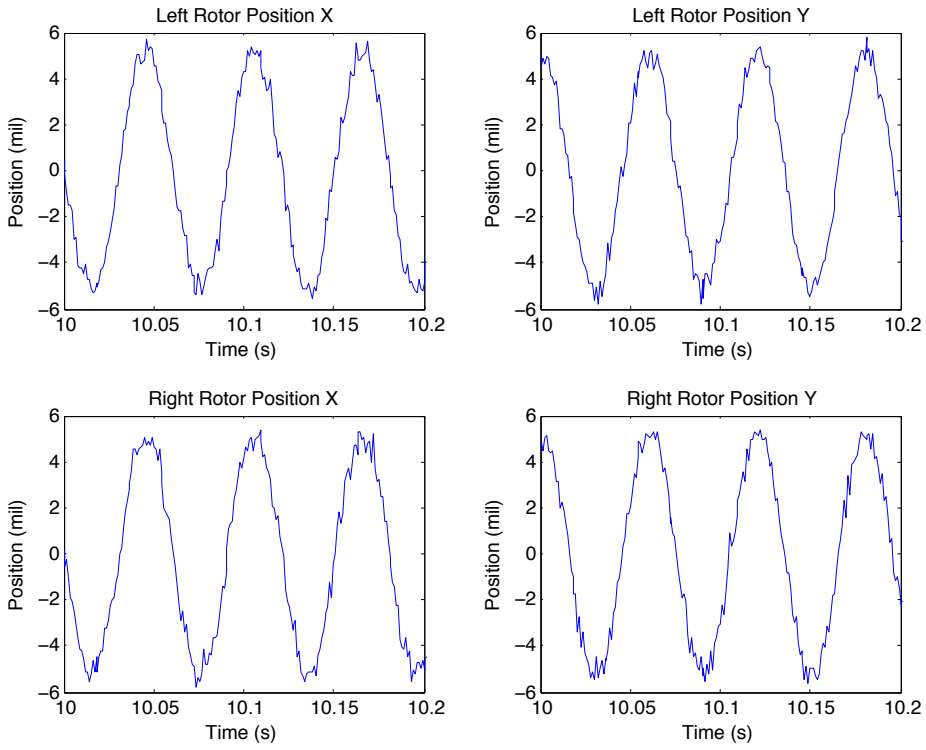

Figure 5.1: Simulated No-Fault Left and Right Rotor Vibration (Detailed View)

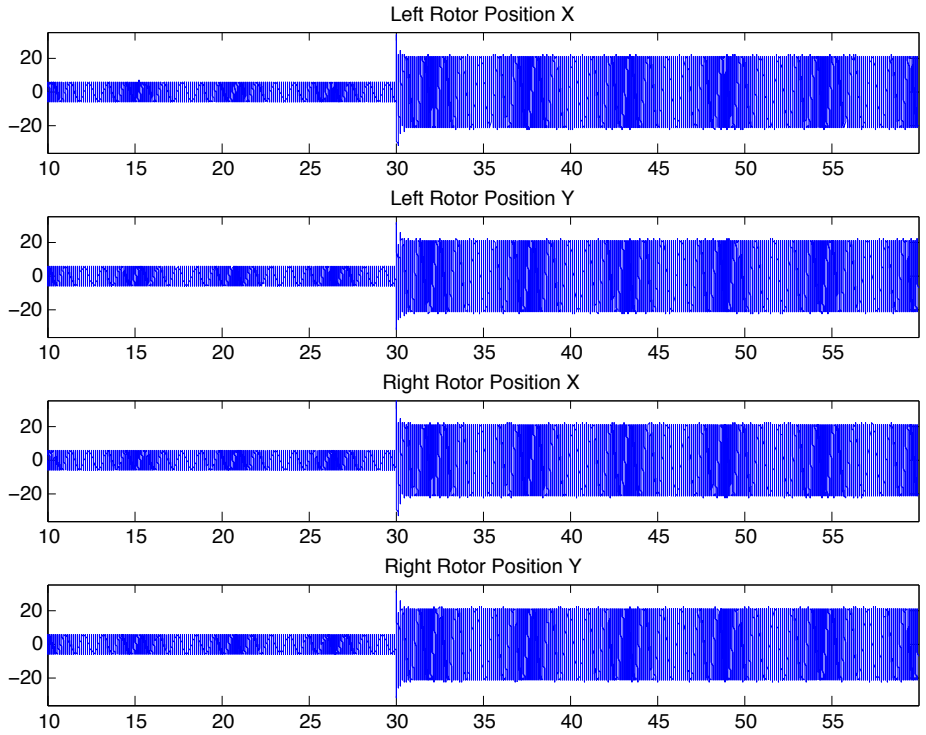

Figure 5.2: Simulated 6 g Static Imbalance Left and Right Rotor Vibration

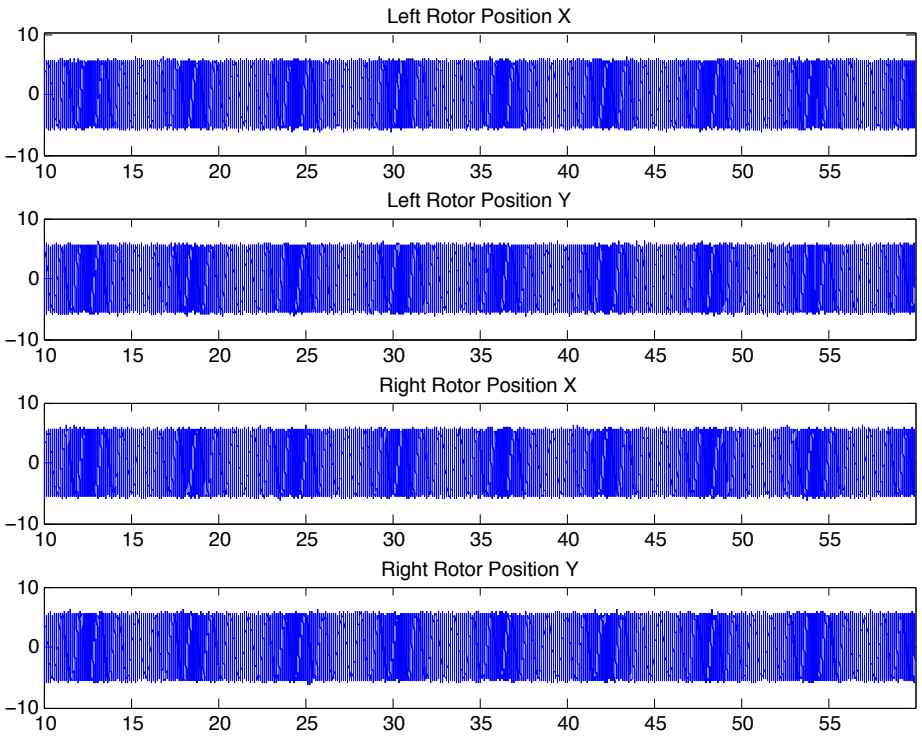

Figure 5.3: Simulated 6 g Dynamic Imbalance Left and Right Rotor Vibration

A five minute simulation for the no-fault system was performed before simulating any faults, to obtain the no-fault residuals necessary to calculate the variance vector. A plot of the no-fault simulation test statistics from this simulation after variance normalization is provided in Figure 5.4.

The residuals were normalized to unit variance using the variance vector calculated from no-fault data, and then a norm-squared test statistic was calculated for each normalized vector. The test statistic was then compared with the threshold value T_r of 35.17 obtained in the previous section. A fault was judged to have occurred whenever the test statistic exceeded the threshold. Results for the simulations are plotted in Figures 5.5 to 5.12. The threshold is superimposed as a dashed horizontal line in each figure.

The fault occurs at 30 s in each simulation. In each case, there is an immediate and observable increase in the magnitude of the test statistic. However, for the faults of smaller magnitude the increase did not necessarily exceed the detection threshold. These results demonstrated the lower limit of detectability for the subspace method.

Figure 5.5 shows the test statistic sequence for a 2 g static imbalance. Although the fault was apparent by subjective analysis, the test statistics were well below the detection threshold. In the subsequent 4 g static imbalance shown in Figure 5.6, the average test

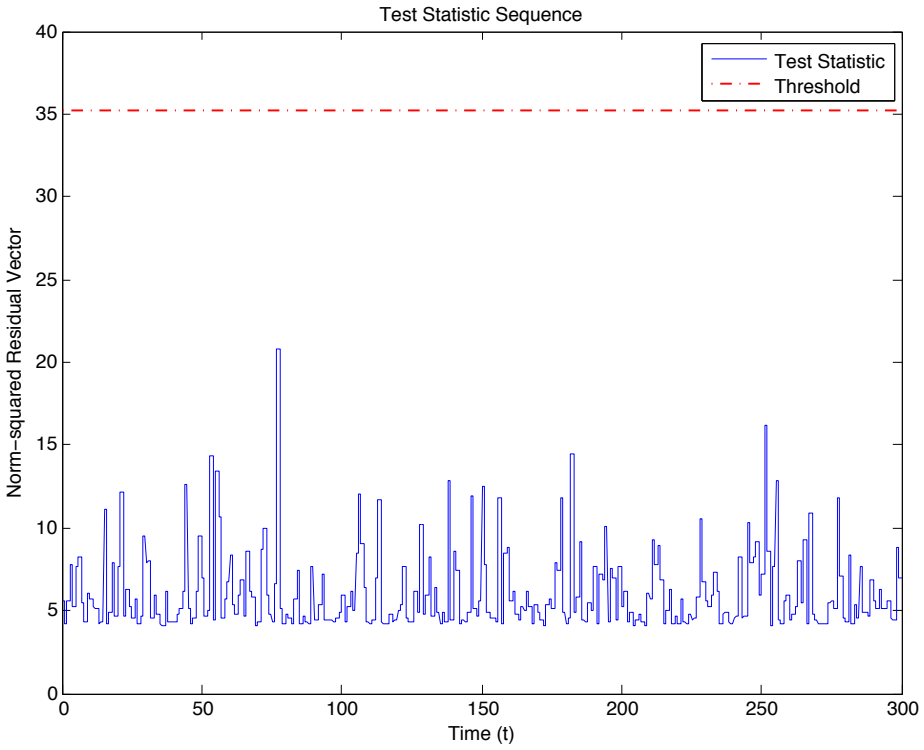

Figure 5.4: Simulated Machine No-Fault Test Statistic Sequence

statistic was slightly above the detection threshold, although there was little margin for many windows. Finally, Figures 5.7 and 5.8 show the sequences for 6 g and 8 g static imbalances, respectively. The post-fault test statistics were all comfortably above the threshold. Taken together, these results demonstrate a 4 g imbalance was the threshold of detectability for a static imbalance.

No false positives were detected during any of the simulations, due to the conservative threshold choice. A more generous threshold would decrease the detectable imbalance mass, but as Figure 5.5 demonstrated, a threshold sufficiently low to detect a 2 g static imbalance would raise the possibility of false positives.

Figures 5.9 and 5.10 show the test statistic sequence for 2 g and 4 g dynamic imbalances, respectively. The 2 g imbalance test statistics were below the detection threshold for the most part, but several windows produced a detectable statistic. The 4 g imbalance produced test statistics that were comfortably above the threshold. This pattern carried forward in the sequences plotted for the 6 g and 8 g imbalances in Figures 5.11 and 5.12. The subspace method was better able to detect dynamic imbalances because as Figures 3.18 and 3.19 illustrated, static imbalances had the effect of altering the magnitude of mode shapes while dynamic imbalances alter their form.

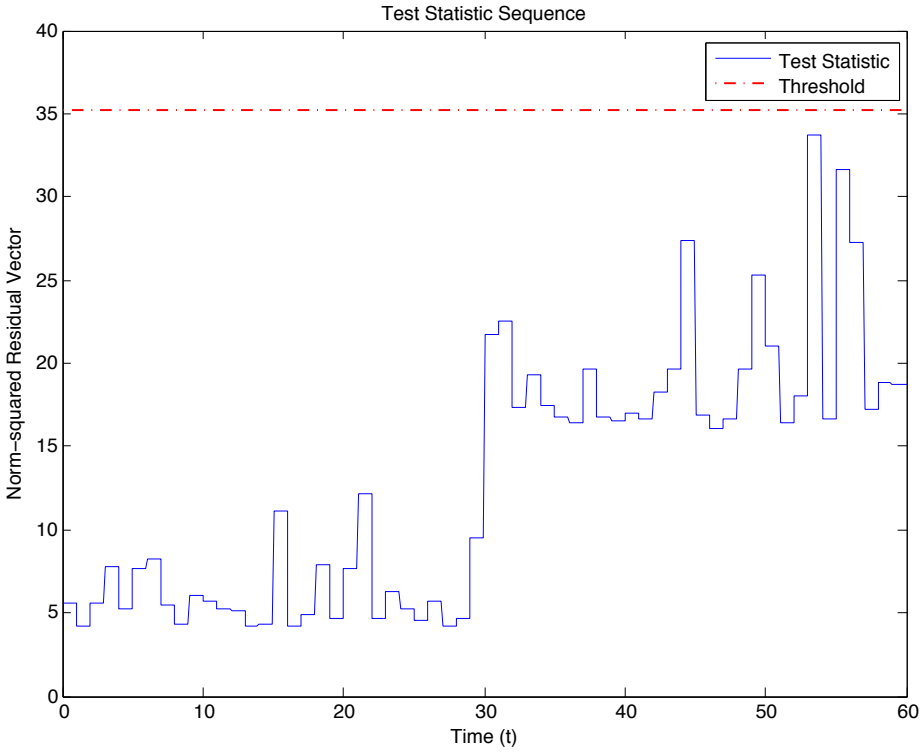

Figure 5.5: Simulated Machine Static Imbalance 2g Test Statistic Sequence

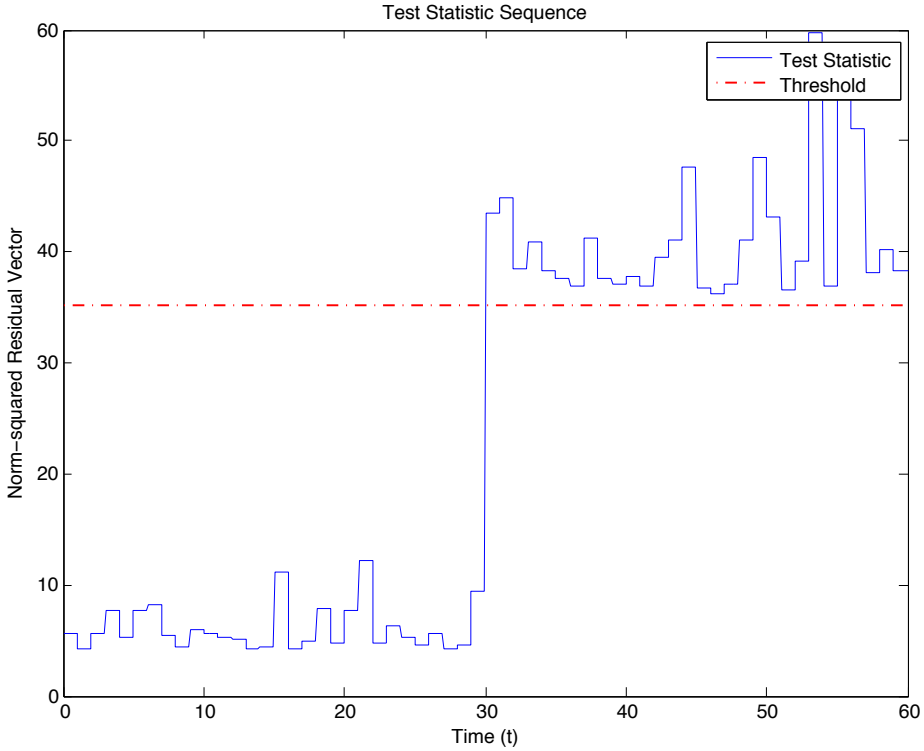

Figure 5.6: Simulated Machine Static Imbalance 4g Test Statistic Sequence

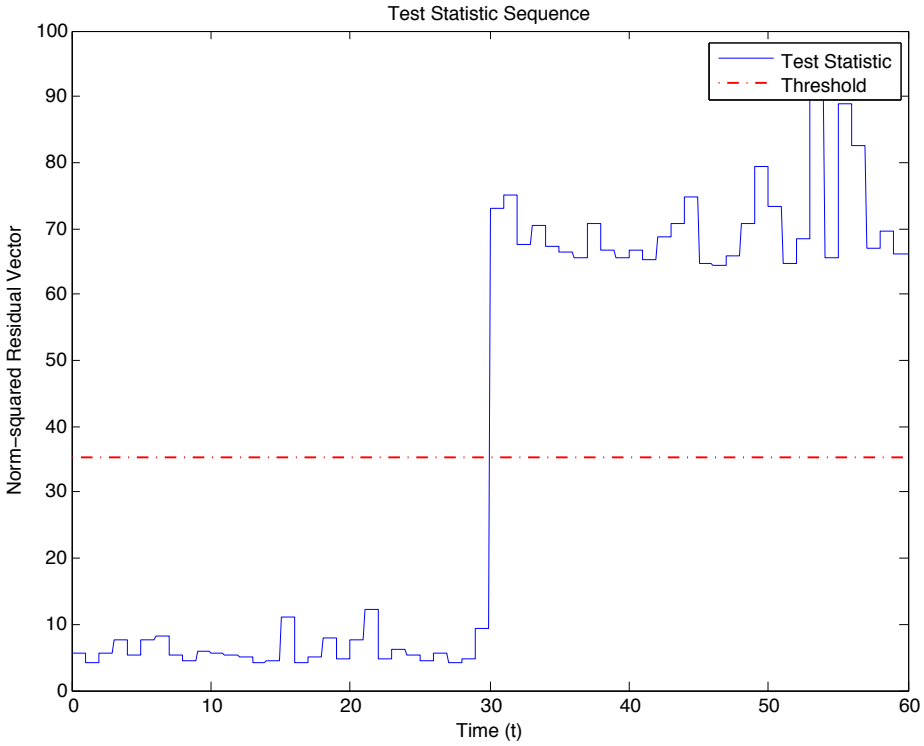

Figure 5.7: Simulated Machine Static Imbalance 6g Test Statistic Sequence

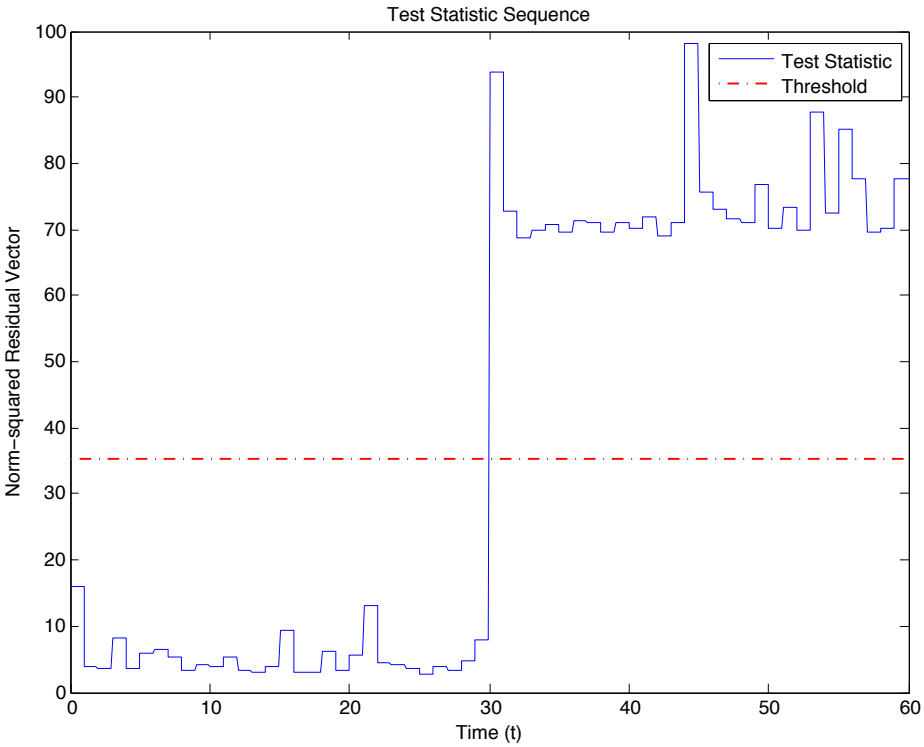

Figure 5.8: Simulated Machine Static Imbalance 8g Test Statistic Sequence

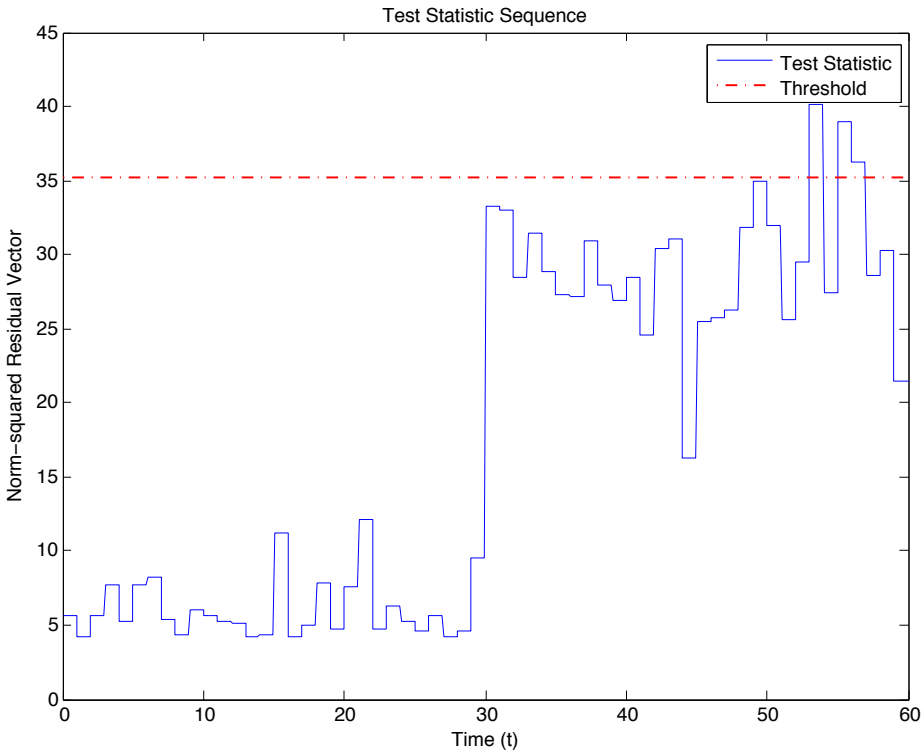

Figure 5.9: Simulated Machine Dynamic Imbalance 2g Test Statistic Sequence

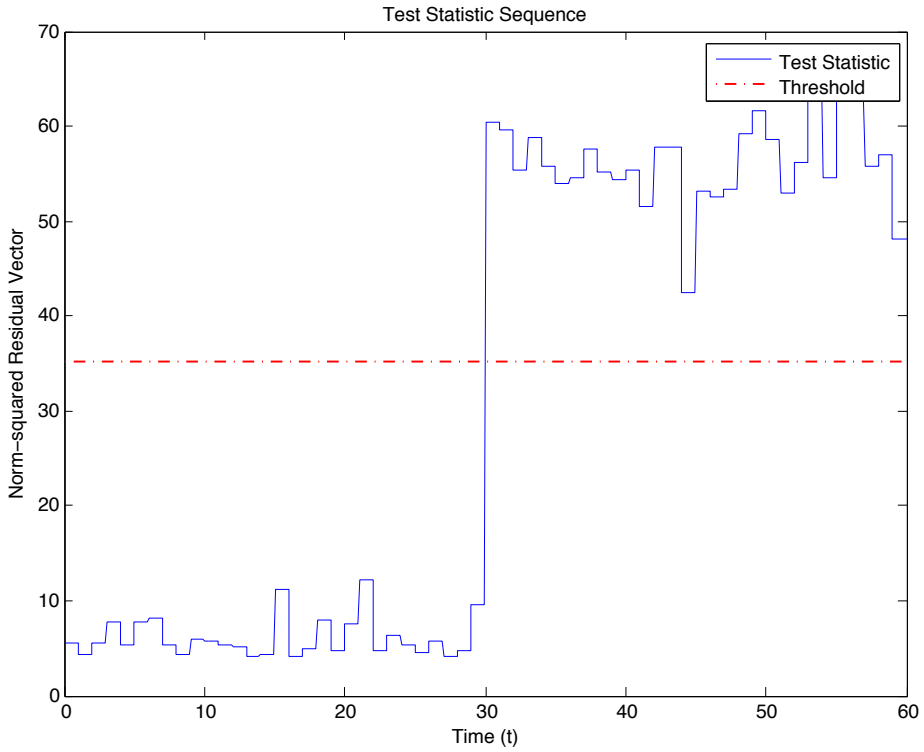

Figure 5.10: Simulated Machine Dynamic Imbalance 4g Test Statistic Sequence

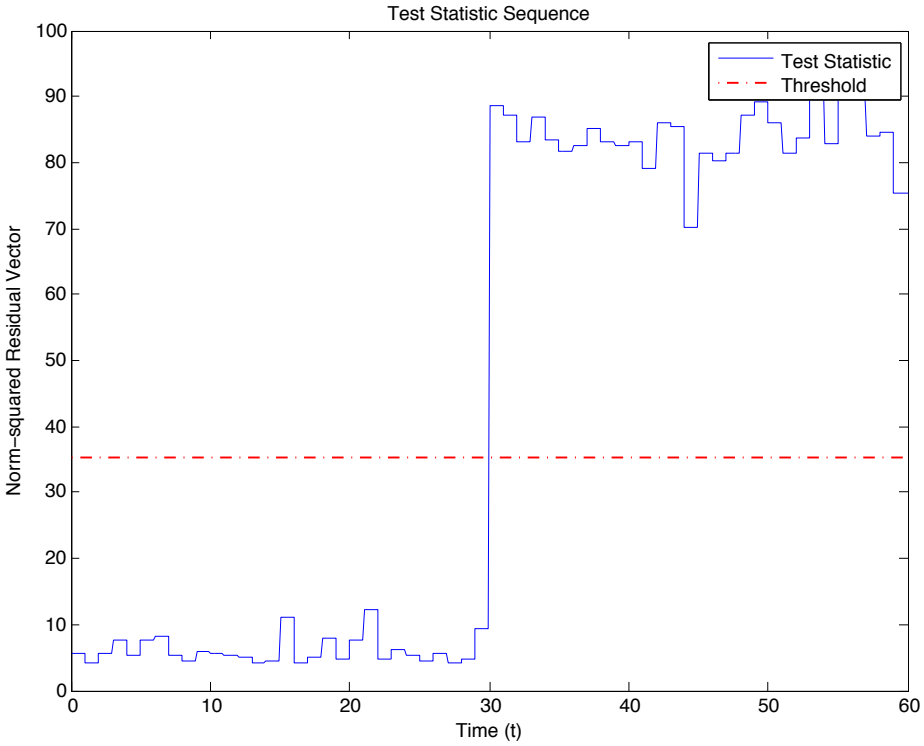

Figure 5.11: Simulated Machine Dynamic Imbalance 6g Test Statistic Sequence

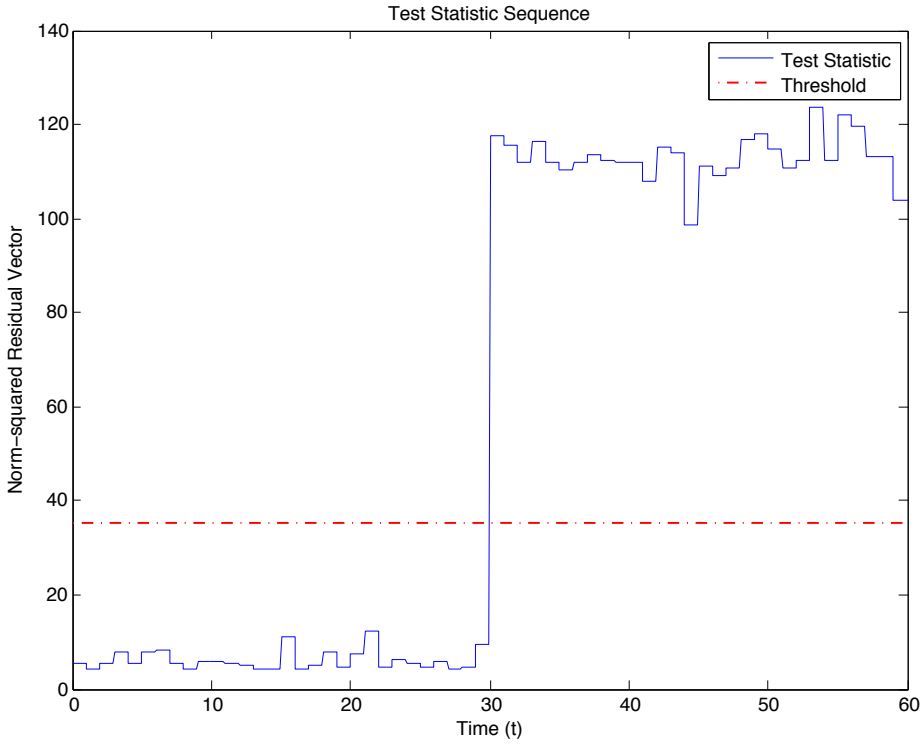

Figure 5.12: Simulated Machine Dynamic Imbalance 8g Test Statistic Sequence

5.2.3 Sinusoidal Synthesis Method

Unlike the subspace method, SS generates a straightforward scalar output residual by subtracting the predicted output from the measured signal. Faults are detected when the magnitude of the residual exceeds a predetermined threshold value. Therefore, unlike the test statistics produced by the subspace method for discrete time windows, SS produces a sequence of residual values for every step in the simulation. Also unlike the subspace method, SS is fundamentally a single-output algorithm and must be applied individually to each output for multiple-output systems.

Simulations were performed for 6 g static and dynamic imbalances, and SS was applied to the x-axis position signal at the left rotor position to generate residual sequences for each simulation. The 6 g faults were selected under the assumption that if SS cannot detect a severe fault, it is unlikely to be effective for more subtle faults.

A design element of the algorithm is the selection of s-plane pole locations for the lambda polynomial. Three pairs of complex conjugate poles were selected to be sufficiently far from the y-axis as to obtain 95% matching of the actual output signal under steady-state conditions.

A drawback of the SS method is that it does not perform well when applied to noisy signals. When significant noise is present, the adaptive procedure will tend to minimize the contribution of the adaptive model and the beta values will quickly converge to zero. Therefore, it was necessary to apply a low-pass filter to the measured signals before applying the algorithm. A low-pass filter with a cutoff frequency of 50 Hz was applied to the measured output signals before application of SS.

Figures 5.13 and 5.14 show comparison plots of the measured output signals for the simulated systems against the corresponding predicted outputs for the 0.5 s preceding and 1.5 s following the introduction of a fault. If the SS residual was going to increase in response to a fault, it would most likely do so within this window. It can be observed from these figures that SS closely tracks the measured signal, even at the moment the fault occurs and significant transient effects are present. Imbalance faults do not alter the fundamentally sinusoidal nature of the vibration signals, unlike the impulsive faults associated with gear and rotor cracking that motivated the development of SS.

5.2.4 Hilbert-Huang Transform Method

The HHT differs from the previous two methods in that it is not an automatic fault detection algorithm, but a series of transformations of the measured output that enables expert

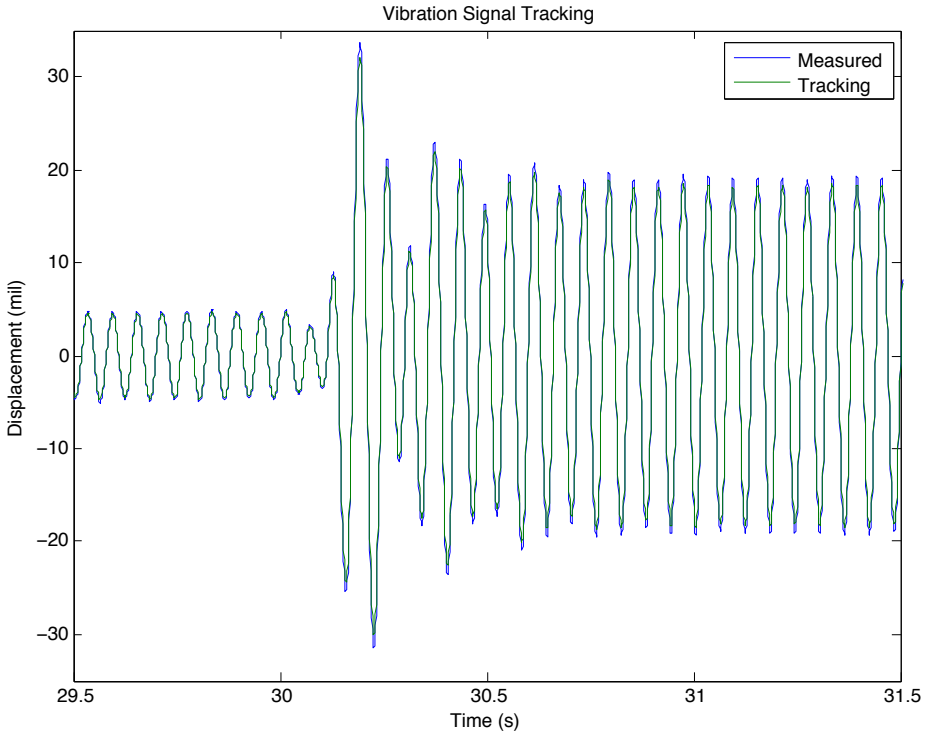

Figure 5.13: Simulated Machine Static Imbalance Sinusoidal Synthesis Tracking

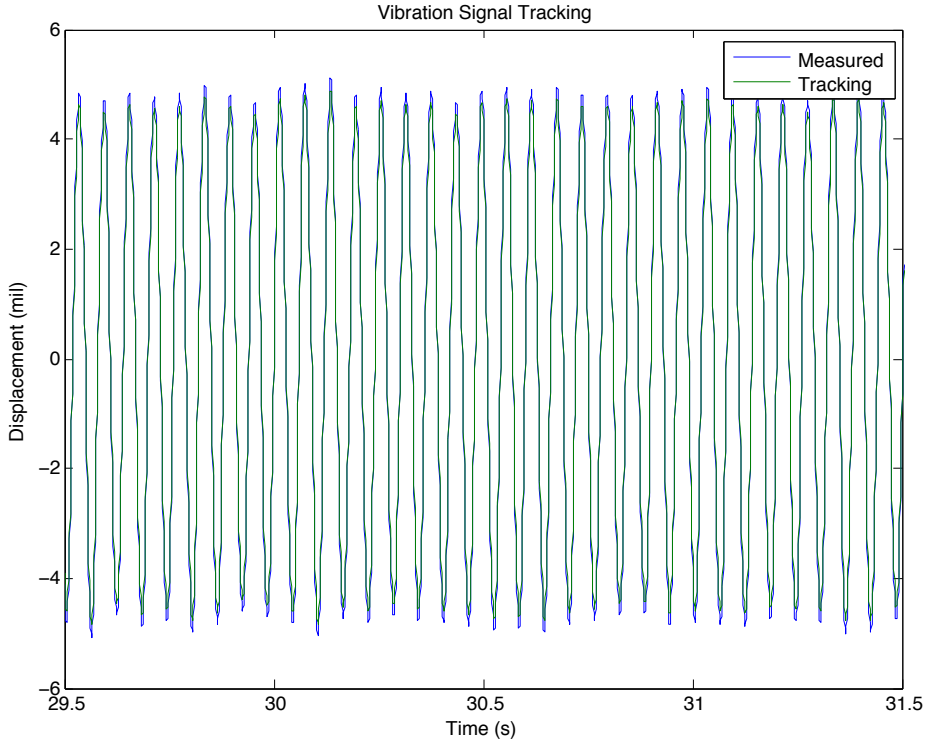

Figure 5.14: Simulated Machine Dynamic Imbalance Sinusoidal Synthesis Tracking

interpretation of the frequency content of the vibration signal as a function of time. For certain types of fault this is a more productive approach than traditional Fourier analysis. The process begins by applying empirical mode decomposition (EMD) to the measured signal, obtaining a set of intrinsic mode functions. (IMFs) This is similar to the Fourier decomposition of a periodic signal into harmonic sinusoidal components, but the IMFs may be more general functions. Most importantly, they are guaranteed to have well-defined Hilbert transformations. Once the IMFs are available, the Hilbert transformation is applied individually to obtain the instantaneous frequency for each IMF, and the results for all IMFs are plotted together as a function of time. Faults are determined by expert analysis of the time-frequency plot. Like SS, this method may only be applied to a single output signal at a time.

Prior to application of the HHT, the vibration signals were filtered using a low-pass filter with a 50 Hz cutoff frequency. This reduced the effect of noise on the HHT results, as physical vibration is largely confined within this frequency range.

Figure 5.15 plots the left rotor x-axis vibration signal, its IMFs, and residue for the 10 s window surrounding the introduction of a 6 g static imbalance. The fault was readily visible as a substantial increase in vibration magnitude starting at 30 s. The majority of the signal energy was contained within the first IMF, whereas the subsequent IMFs appear to represent transient effects occurring at the moment the fault is introduced. Figure 5.16 shows the time-frequency plot obtained by Hilbert transformation of the IMFs. In this figure, the energy content of the signal at a particular time and frequency is represented by color, with low magnitudes at the blue end of the spectrum and high magnitudes at the red end. The fault was also apparent in this figure, as the higher vibration magnitude is clearly visible in yellow-red intensity following the 30 s mark. However, the HHT does not provide any particular insight into the fault other than to provide an alternative representation of increased vibration magnitude.

Figure 5.17 shows the left rotor x-axis vibration signal, IMFs, and residue for the 10 s window surrounding introduction of a 6 g dynamic imbalance. Compared with the previous example, it was difficult to observe that any fault has occurred. The first IMF contained the majority of the signal energy, and no transient effects were observed in subsequent IMFs corresponding to the fault occurrence. Figure 5.18 contains the time-frequency plot for the HHT of these IMFs. Again, there was little observable difference between the no-fault half of the simulation and the time-frequency plot following the fault.

HHT does not appear to provide any advantage for imbalance fault detection.

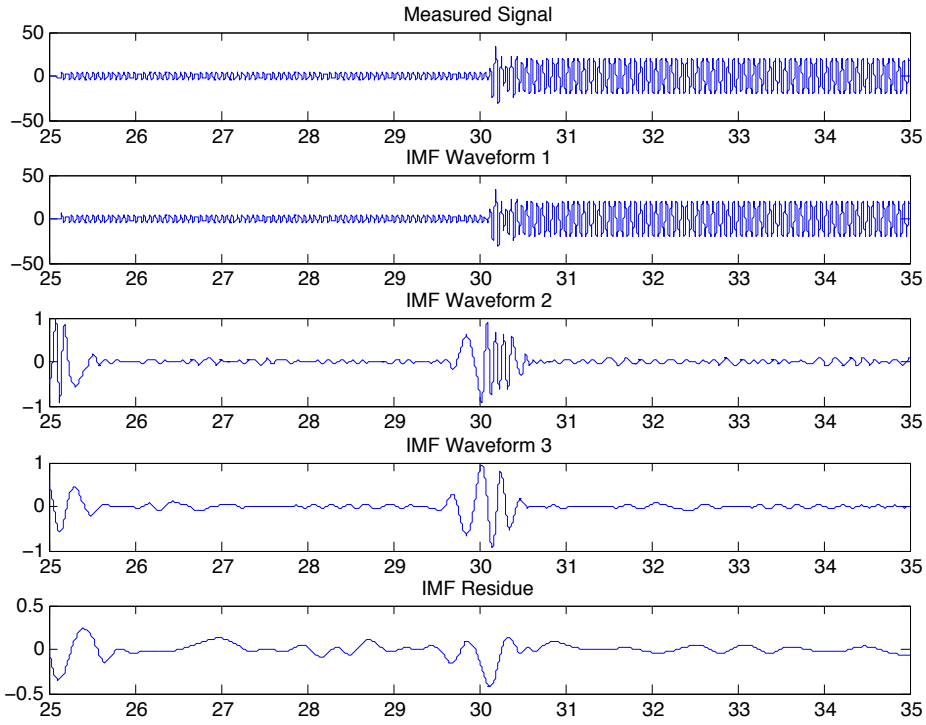

Figure 5.15: Simulated Machine Static Imbalance Left Rotor Vibration IMFs

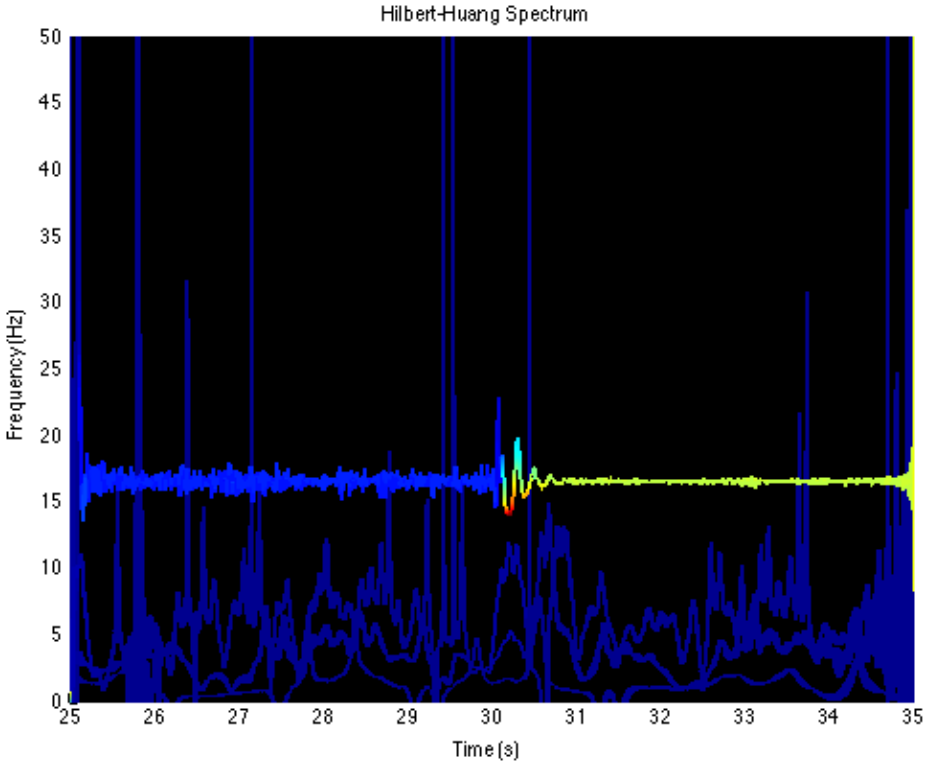

Figure 5.16: Simulated Machine Static Imbalance Left Rotor Vibration HHT

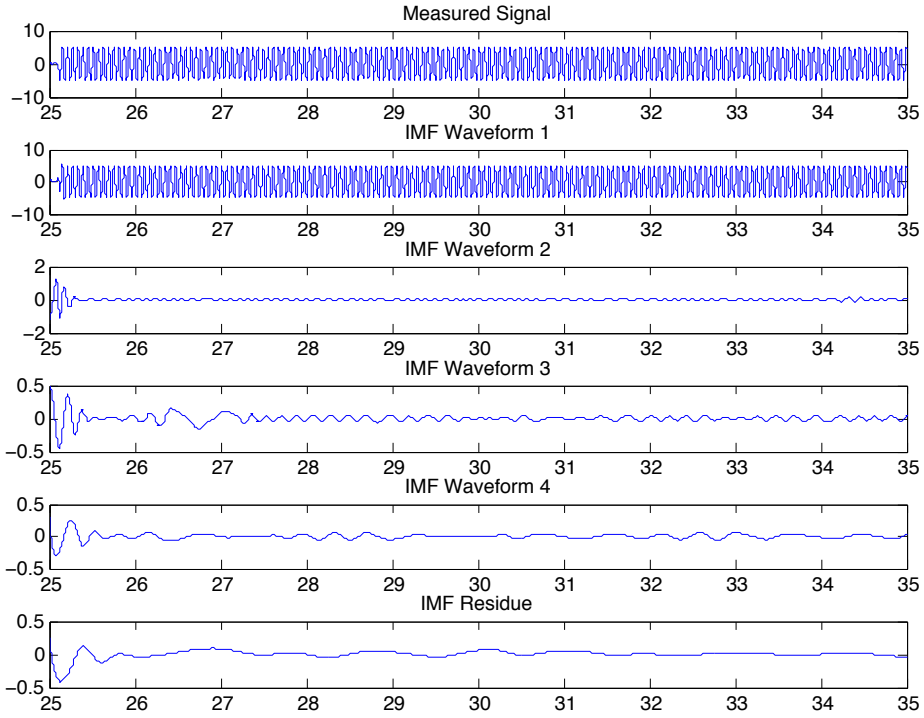

Figure 5.17: Simulated Machine Dynamic Imbalance Left Rotor Vibration IMFs

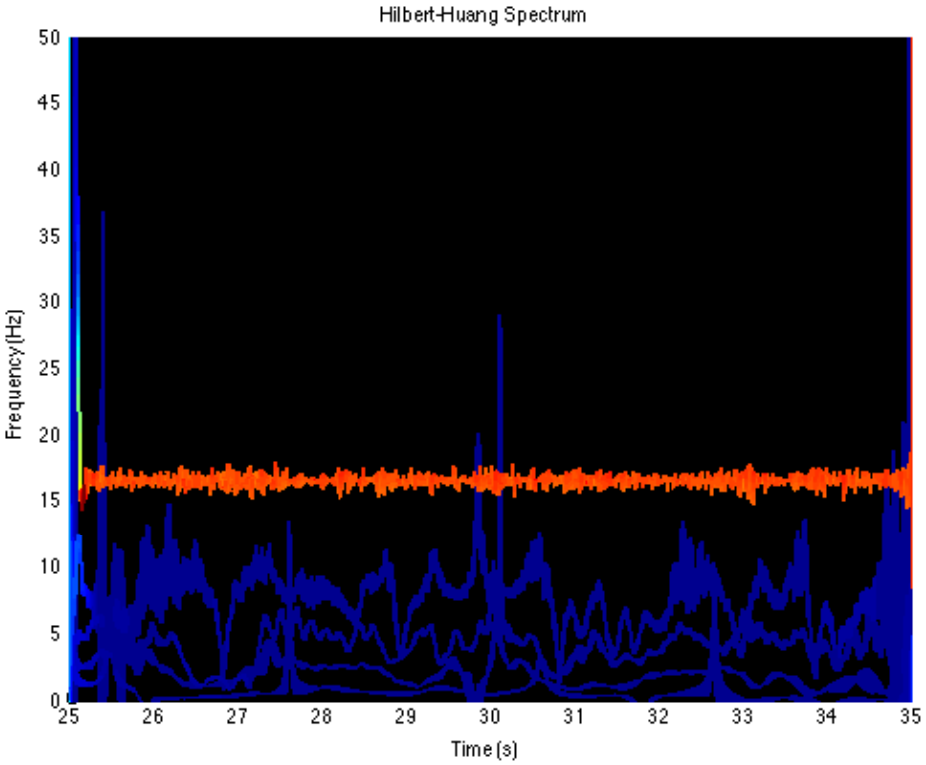

Figure 5.18: Simulated Machine Dynamic Imbalance Left Rotor Vibration HHT

5.3 Physical Machine Fault Detection

The physical machine provided an opportunity to test the subspace fault detection method on a system with more complex dynamics and limited instrumentation. Although the simulation and physical machine were designed to be as similar as possible, comparison of the ramp-up tests in Figures 3.12 and 3.12 demonstrates that the simulation could only approximate the physical machine. Unlike the simulation, only two position sensors were available for the physical machine. The simulation also benefited from the ability to introduce faults of any size or location at any time during a test run, whereas tests conducted on the physical machine necessarily had a fault present or absent for the entire run as it was impossible to attach weights while the machine was in operation.

Each test on the physical machine was conducted at a constant operating speed of 1000 RPM. Static imbalances were created by attaching a 10 g weight to the center flywheel at 0° on the inner or outer attachment rings. The 0° position was defined as the position of the setscrew holding the flywheel on the rotor, as these were aligned to the same position on the shaft for all three flywheels. Dynamic imbalances were created by attaching weights at 0° and 180° on the right and left flywheels, respectively, with both weights placed either on the inner or outer attachment rings.

5.3.1 Subspace Method

Using the machine model and the intermediate calculations described earlier, residual vectors were calculated for 1 s windows at corresponding intervals throughout each test run using the x-axis position signals at the left and right rotor positions. A five minute test run for the no-fault system was performed first, to obtain the no-fault residuals necessary to calculate the variance vector. A plot of the no-fault test statistics from this run is included in Figure 5.19. As was obvious through comparison of the critical speeds in Figures 3.12 and 3.21, the simulated and physical machines were not identical. The no-fault machine model was calculated to precisely match the simulation, and so the small discrepancy with the physical machine explains the decrease in effectiveness shown by the subsequent physical subspace method results. The subspace fault detection method does not require a perfect no-fault model, but its effectiveness decreases as the discrepancy between model and machines grows.

The residuals were normalized to unit variance using the variance vector calculated from no-fault data, and then a norm-squared test statistic was calculated for each normalized

vector. The test statistic was then compared with the threshold value T_r of 35.17 obtained earlier. When the test statistic exceeded the threshold, a fault has judged to have occurred. Results for the simulations are plotted in Figures 5.20 to 5.23. The threshold is superimposed as a dashed horizontal line in each figure.

Unlike the simulation, the physical machine was not capable of introducing a fault during the middle of a test run. As a result, in all four test runs that were conducted with a fault present there was an immediate rise in the test statistic above the threshold as the machine ramped up to operating speed. It can be see in Figure 5.19 that a single false positive was observed during startup in the no-fault test, and that each of the fault cases had inconsistent behavior during startup. The machine experienced a significant amount of transient behavior and traversed critical speeds during ramp-up, so results prior to steady-state operation should be disregarded. All four test runs with fault conditions produced unambiguous results, with the test statistic well above the detection threshold after the initial ramp-up period.

Figures 5.20 and 5.21 show the test statistic sequences for static imbalances created by attaching 10 g weights to the inner and outer attachment rings on the center flywheel, respectively. Both positions produced significant vibration, and the test statistics were well above the detection threshold. The physical machine was not capable of producing static imbalances small enough to determine the minimum detectable fault for this setup.

Figures 5.22 and 5.23 show test statistic sequences for dynamic imbalances created by attaching 10 g weights to the inner and outer attachment rings on the outer flywheels, respectively. The effect was more subtle than the static imbalances cases, although both faults were easily detected. It was not possible to create a smaller dynamic imbalance, but the results for the inner attachment ring suggested that a 10 g inner imbalance was close to the minimum detectable fault for this setup.

Despite the model-machine discrepancy, the subspace fault detection method was capable of detecting physical machine faults of both types and severities, and did not return false positives when applied to the no-fault machine. These results confirm the validity of the simulation and the potential for applying this algorithm to practical machines.

5.3.2 Sinusoidal Synthesis Method

The SS method was applied to the experimental data collected from the physical machine for the static and dynamic imbalances with 10 g weights on the outer attachment rings. Unlike the simulated results, the faults could not be introduced in the middle of a test run,

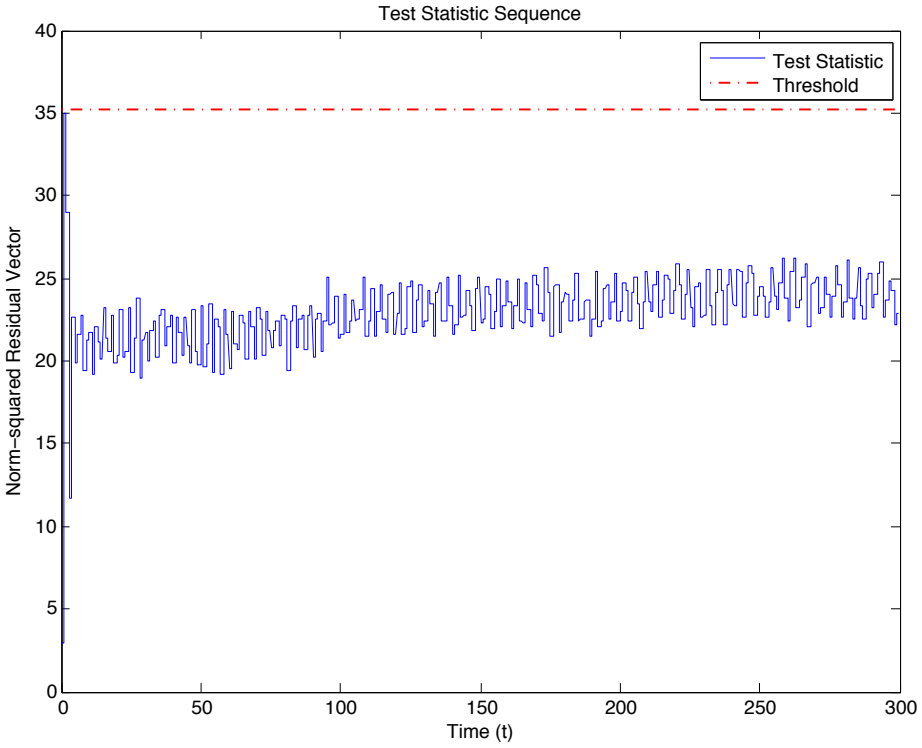

Figure 5.19: Physical Machine No-Fault Test Statistic Sequence

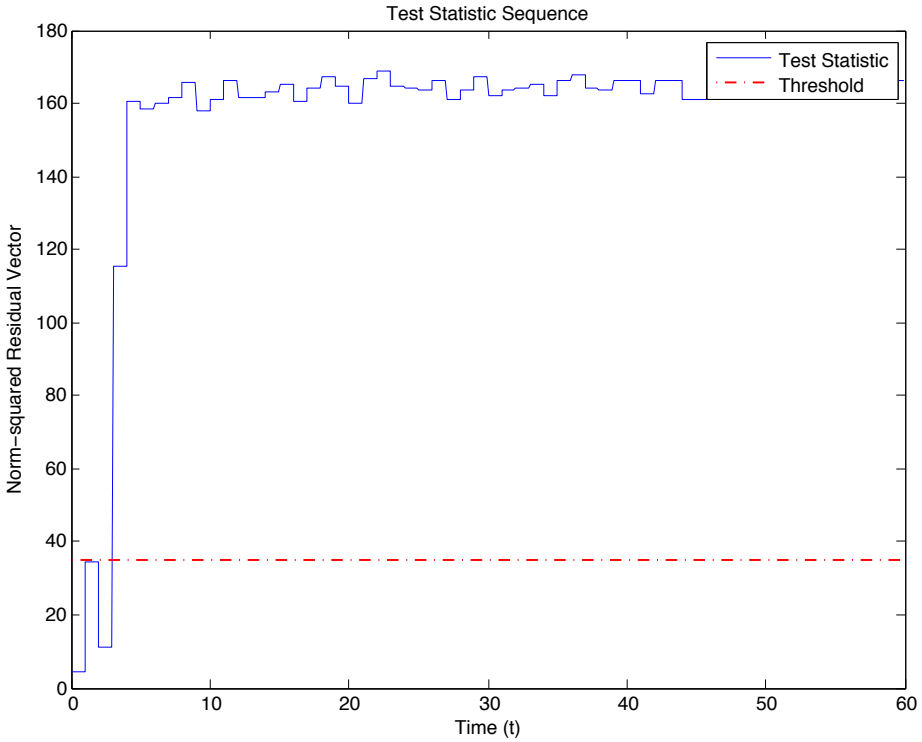

Figure 5.20: Physical Machine Inner Static Imbalance Test Statistic Sequence

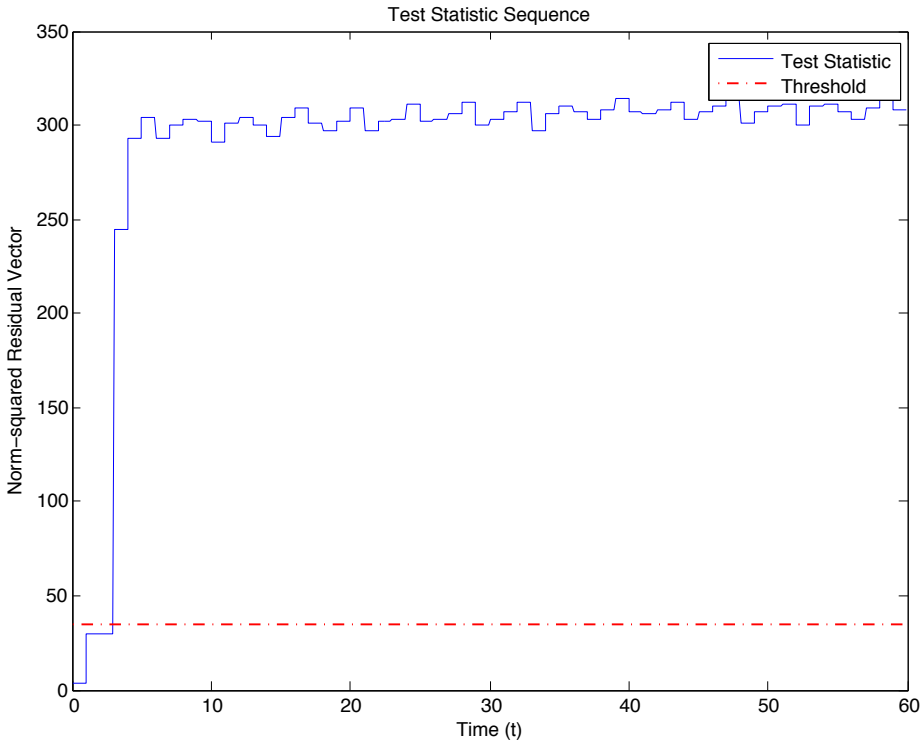

Figure 5.21: Physical Machine Outer Static Imbalance Test Statistic Sequence

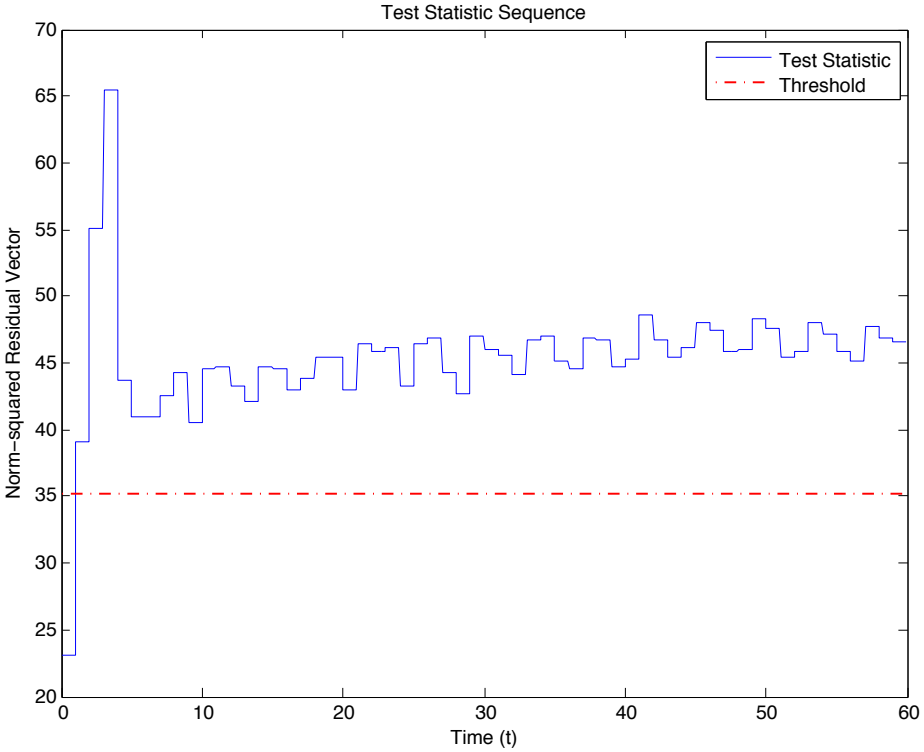

Figure 5.22: Physical Machine Inner Dynamic Imbalance Test Statistic Sequence

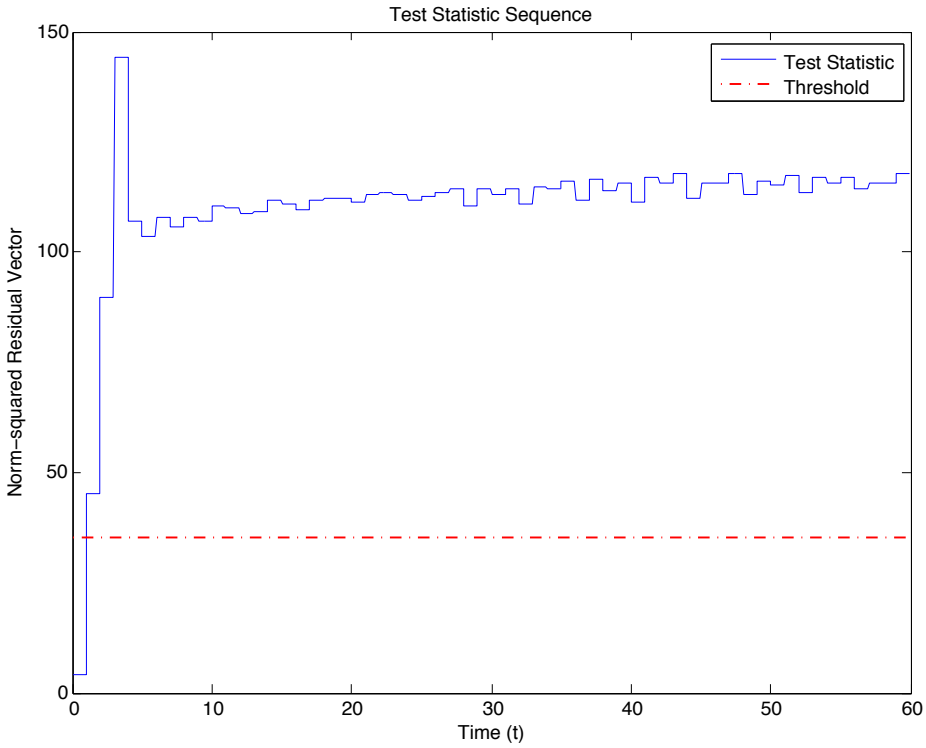

Figure 5.23: Physical Machine Outer Dynamic Imbalance Test Statistic Sequence

so faults were present for the entire test. The pole locations selected for the simulation data were used to generate these results. A low-pass filter application was not necessary in this case, as a low-pass filter was applied as part of the decimation process to reduce the 10 kHz laboratory data to 1 kHz for analysis.

Figures 5.24 and 5.25 contain comparison plots of the measured output signals for the physical system against the corresponding predicted outputs, in close-up. Detection of an error is possible when the measured output is significantly different from the SS prediction. It can be observed in these figures that SS closely tracks the measured signal at all times. Imbalance faults do not alter the fundamentally sinusoidal nature of the vibration signals, and without being able to observe the moment of fault introduction the SS method is even less effective when applied to the physical machine.

5.3.3 HHT Method

The HHT was applied to the vibration data collected for the 10 g outer static and dynamic imbalances. The results, along with an HHT of a 60 s no-fault test run, are provided in Figures 5.26 to 5.31. As it was impossible to introduce a fault while the machine was in operation, the best way to illustrate the difference between the three cases was to plot the

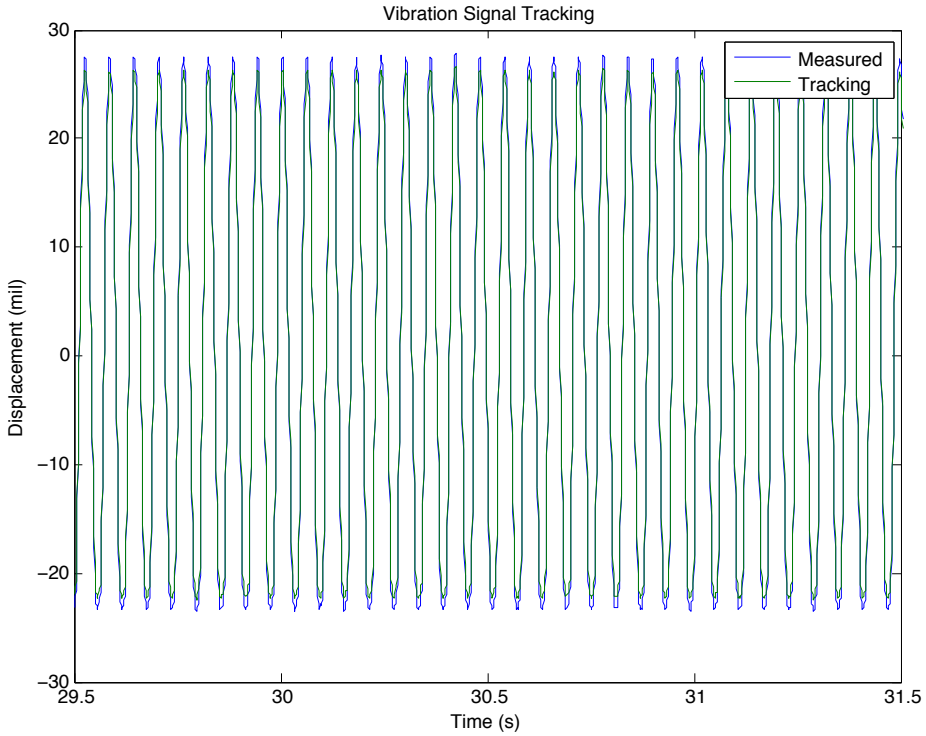

Figure 5.24: Physical Machine Static Imbalance Sinusoidal Synthesis Tracking

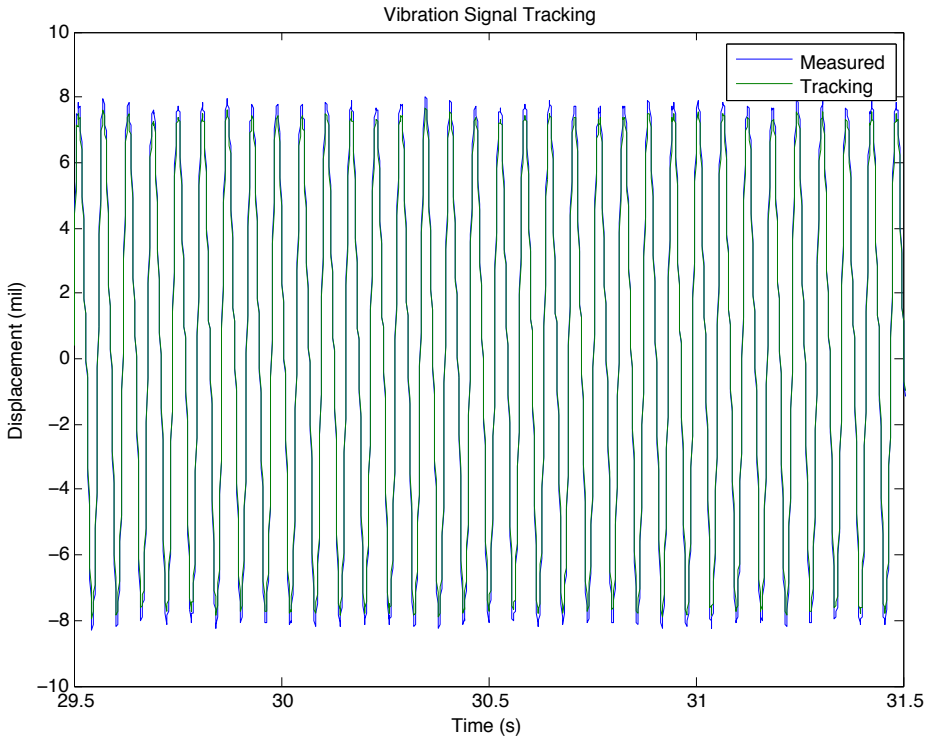

Figure 5.25: Physical Machine Dynamic Imbalance Sinusoidal Synthesis Tracking

IMFs and a representative selection of the HHT. If the HHT was effective at discriminating between no-fault and fault cases, it would be apparent from comparison of the no-fault and fault figures.

Figures 5.26, 5.28, and 5.30 plot the IMFs for the no-fault, static imbalance, and dynamic imbalance cases, respectively. It can be observed from these figures that in each case the original vibration signal is approximately sinusoidal due to the dominant 1X component, so that the EMD produced a single dominant IMF followed by a collection of insignificant transient IMFs. There was no obvious distinction between the no-fault and fault cases.

Figures 5.27, 5.29, and 5.31 show the HHT plots for each of the previous cases. Without the transient effects present in the simulation HHT results, determining the presence of a fault was even more difficult. The only distinguishing feature between the no-fault case and the static imbalance was the greater intensity of vibration, as reflected in the magnitude of the first IMF in Figure 5.28 and the red shift in Figure 5.29. There was no observable difference between the no-fault and dynamic imbalance cases.

These results showed the HHT to be an even less effective fault detection tool for the physical machine than it was for simulation. At best, as with the static imbalance, they illustrated an obvious difference in vibration magnitude by another means. The subspace fault detection method was far more effective, particularly for dynamic imbalances.

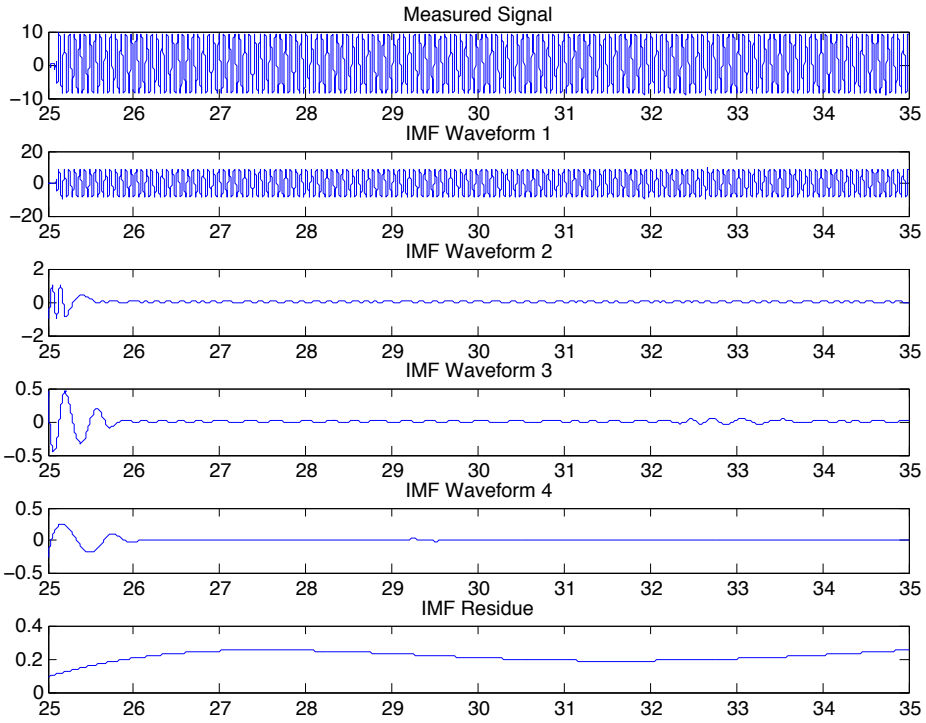

Figure 5.26: Physical Machine No Fault Left Rotor Vibration IMFs

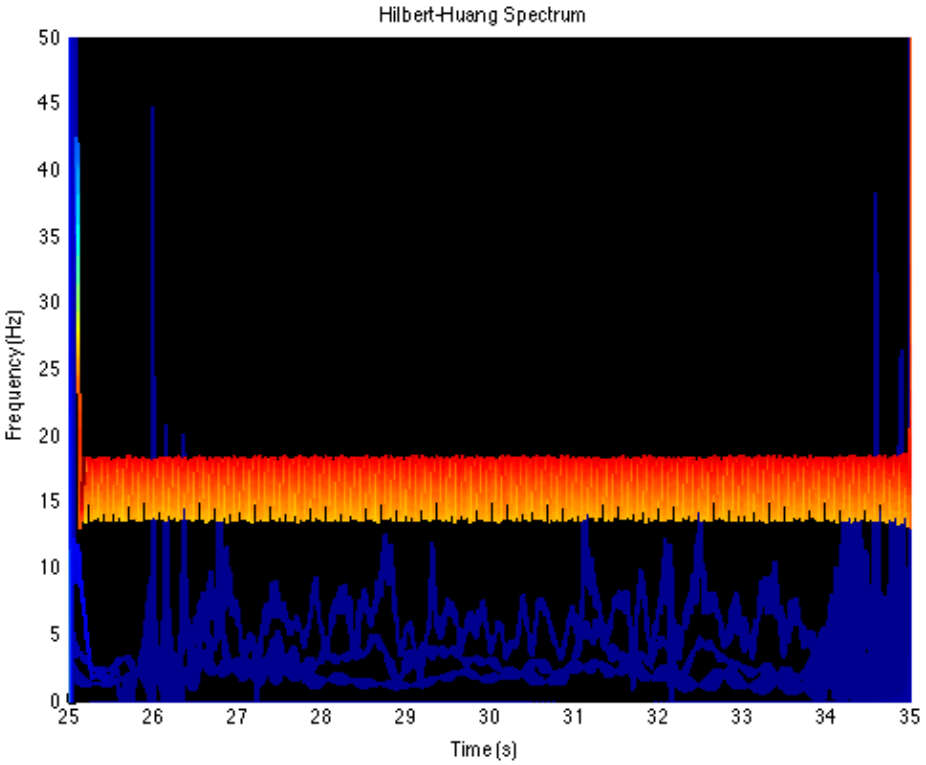

Figure 5.27: Physical Machine No Fault Left Rotor Vibration HHT

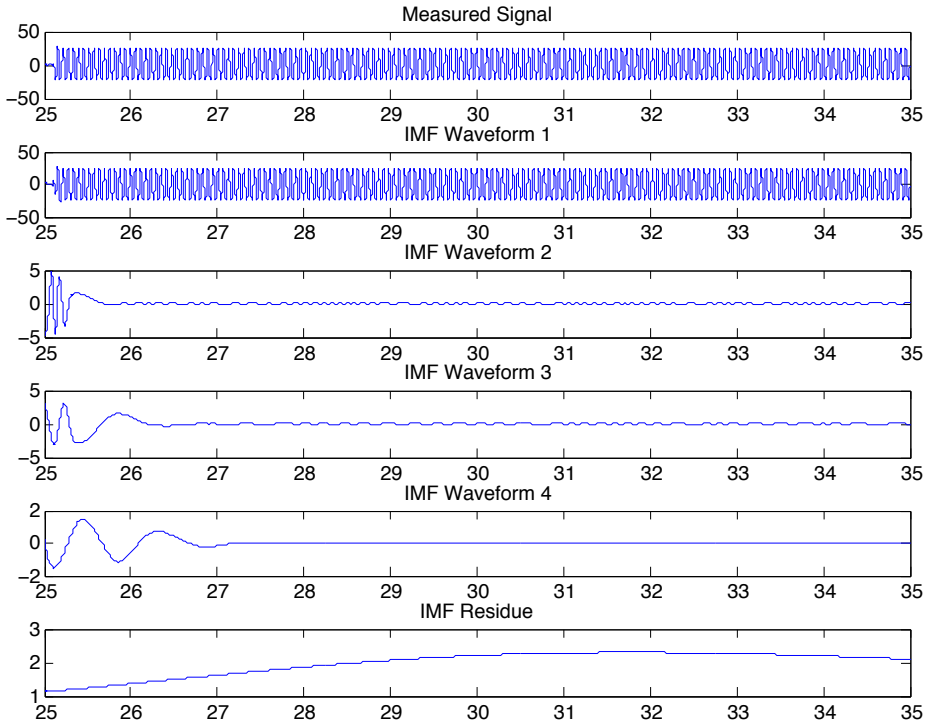

Figure 5.28: Physical Machine Static Imbalance Left Rotor Vibration IMFs

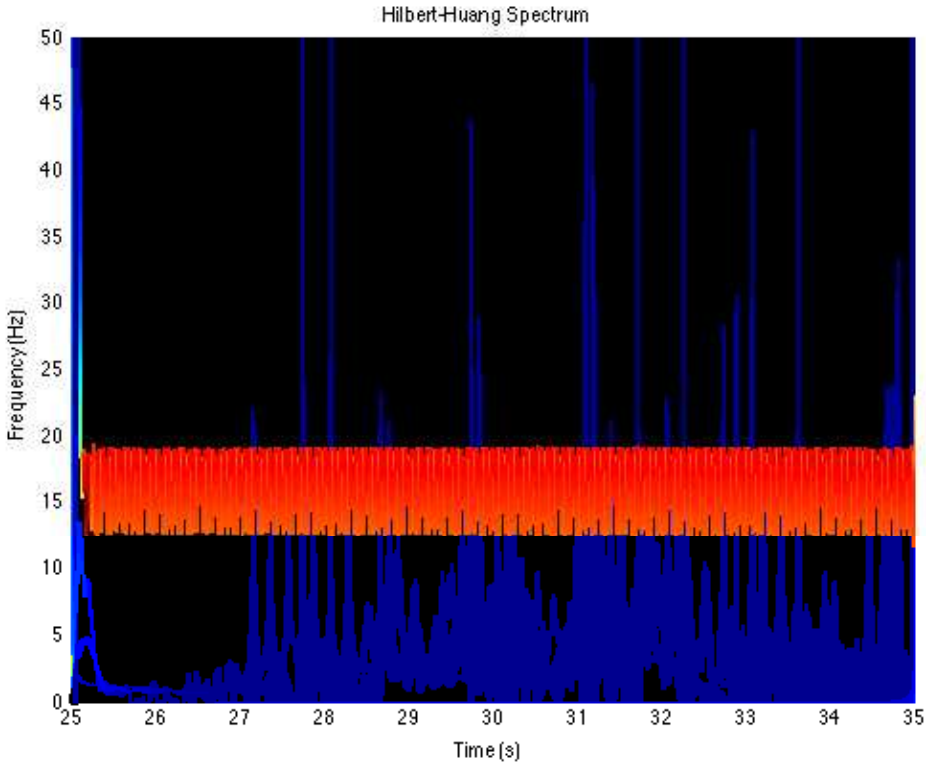

Figure 5.29: Physical Machine Static Imbalance Left Rotor Vibration HHT

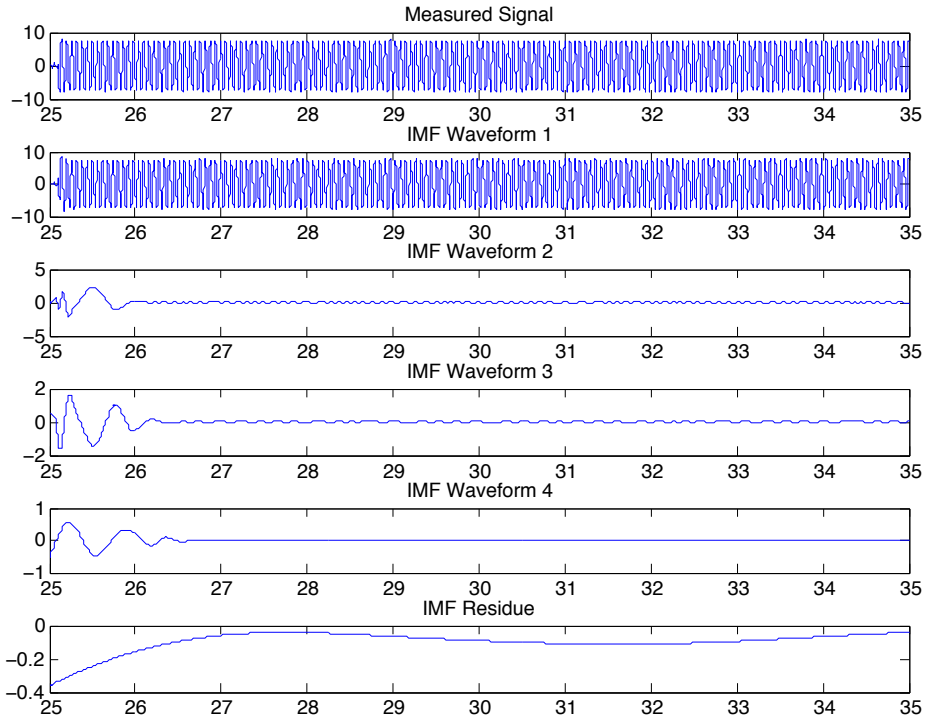

Figure 5.30: Physical Machine Dynamic Imbalance Left Rotor Vibration IMFs

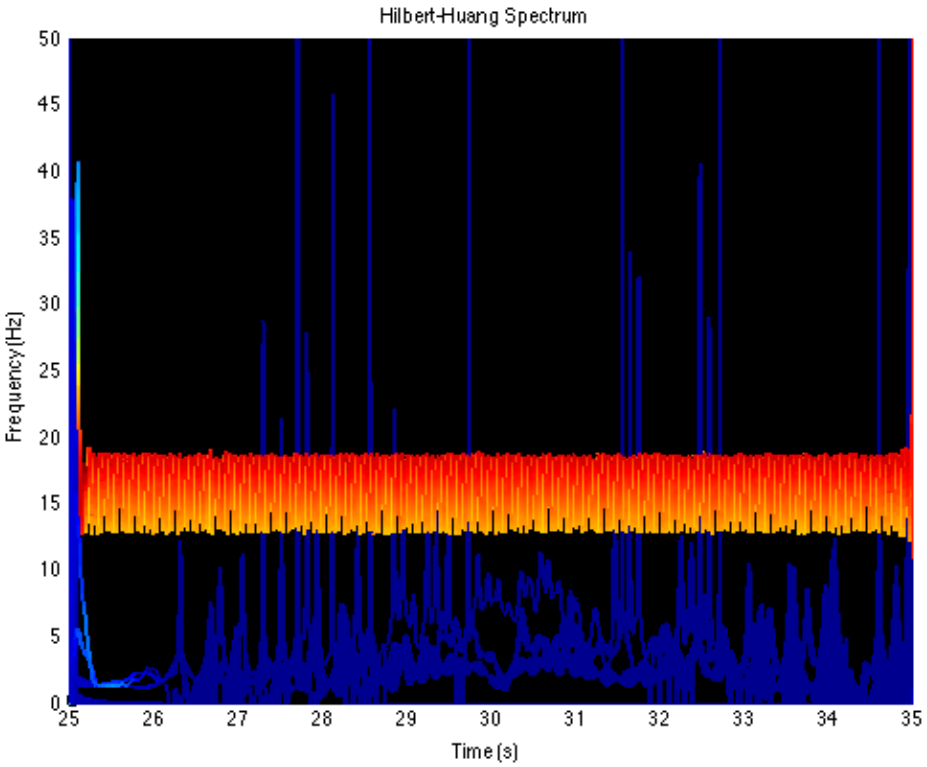

Figure 5.31: Physical Machine Dynamic Imbalance Left Rotor Vibration HHT

Chapter 6

Summary and Future Directions

6.1 Summary

Much attention has been paid to the detection of rotating machine faults in general, but little has concerned quickly-developing imbalance faults like those experienced by centrifugal separators. This is a relatively uncommon type of fault in comparison with gear and rotor cracking, or bearing failure, which together represent a significant proportion of all rotating machine failures. Static imbalances are often simple to detect as they tend to manifest as significantly elevated vibration levels, lending themselves to diagnosis by expert analysis or any number of filtering-based methods. The static imbalance results generated using the HHT method for this thesis demonstrated how easily a significant magnitude change could be detected. Dynamic imbalances are more challenging. As has been demonstrated, dynamic imbalances may have little effect on observable vibration magnitude even though they may have a pronounced effect on the physical deflection of a flexible rotor.

This thesis presented a subspace-based fault detection method that was suitable for detecting both static and dynamic imbalance faults for rotating machines. This method was applied to simulated and physical idealized test machines, and found to be effective for both fault types on scales comparable to the residual rotor imbalance. The subspace method was contrasted with a time-domain sinusoidal synthesis algorithm, and a method based on human interpretation of the time-frequency content of the vibration signals, the Hilbert-Huang transform. The subspace method was at least as effective at detecting static imbalances, and substantially superior when applied to dynamic imbalances. In the latter case, even expert human interpretation of the vibration signals in the time and frequency domains did not easily reveal a fault, whereas the subspace method readily succeeded.

6.2 Major Thesis Contributions

Chapter 3 presented the design and vibration analysis of two idealized rotating machine models intended for the production of controlled static and dynamic imbalances. The first was a simulated physical model implemented in Simulink and SimMechanics, incorporating both linearized bearing simulation and flexible rotor dynamics derived from FEA of the rotor. A physical apparatus based on the simulated machine was constructed in the lab and shown to provide a more realistic environment for testing the subsequent fault detection algorithms.

Chapter 4 presented a version of the Basseville subspace fault detection algorithm applied to constant-speed rotating machines, and demonstrated the calculation of prerequisite computations for the no-fault system model and test statistics from measured data.

Chapter 5 presented a comprehensive set of simulated and physical results for the subspace method and comparison algorithms for a range of static and dynamic imbalance faults. The challenge of detecting dynamic imbalances in particular was illustrated, as was the particular effectiveness of the subspace method for detecting this type of fault.

6.3 Directions for Future Research Studies

The results presented in this thesis involve two main contributions: the idealized rotating machine models and the subspace fault detection method that used them. Each aspect could benefit from future development.

The results of the critical speed tests demonstrated that the simulated machine was a only simplified approximation of the physical apparatus. Despite the idealized nature of both machines, the physical machine was subject to far more complex nonlinearities, noise sources and unmodeled behaviours that could be incorporated into future refinements of the simulation. In addition, the inductive proximity sensors were a luxury that most practical machines lack. In most cases, industrial machines are limited to a small number of accelerometers with poor sensitivity to rotor vibration. Both the machine models and the fault detection algorithm could benefit from further development with more realistic instrumentation.

Modal analysis of real-world machines presents the largest practical challenge to application of the subspace method, and in fact all model-based methods that require a predetermined no-fault model. Even in the case of the idealized models used for this thesis, it was not practical to obtain the model without intimate foreknowledge of the machine

design. Further work toward techniques for matching the identified model to a particular physical machine will be necessary before the subspace method can be applied to real-world problems.

The idealized machines also represent significantly less complex machines than the centrifugal separators that originally motivated this thesis. Practical separators are much more complex, contain a liquid working phase with fluid dynamics, and often use a vertical rotor configuration that substantially alters the flexible rotor and bearing models. The idealized machines represent an excellent starting point, but significant changes may be required to address the challenges of vertical-rotor machines.

References

[1] V. Chudnovsky, A. Mukherjee, J. Wendlandt, and D. Kennedy, "Modeling flexible bodies in SimMechanics," *MATLAB Digest*, May 2006, [Online] http://www.mathworks.com/company/newsletters/articles/modeling-flexible-bodies-in-simmechanics-and-simulink.html.

[2] R. B. Randall, "State of the art in monitoring rotating machinery - part 1," *Sound and Vibration*, vol. 38, no. 3, pp. 14–20, Mar. 2004.

[3] M. L. Adams, *Rotating Machinery Vibration: From Analysis to Troubleshooting*. New York, NY: Marcel-Dekker, 2001.

[4] S. L. Marple, *Digital Spectral Analysis with Applications*. New York, NY: Prentice Hall, 1987.

[5] S. Ding, *Model-Based Fault Diagnosis Techniques: Design Schemes, Algorithms, and Tools*. London, England: Springer-Verlag, 2008.

[6] S. Edwards, A. W. Lees, and M. I. Friswell, "Fault diagnosis of rotating machinery," *Shock and Vibration Digest*, vol. 30, no. 1, pp. 4–13, Jan. 1998.

[7] P. Jayaswal, A. K. Wadhwani, and K. B. Mulchandani, "Machine fault signature analysis," *International Journal of Rotating Machinery*, vol. 2008, 2008, Article ID: 583982.

[8] A. A. Shabana, *Theory of Vibration: An Introduction*. Heidelberg, Germany: Springer-Verlag, 1996.

[9] J. N. Reddy, *An Introduction to the Finite Element Method*. New York, NY: McGraw-Hill., 2005.

[10] K. J. Bathe, *Finite Element Procedures*. Cambridge, MA: Prentice-Hall, 2006.

[11] I. Bucher and D. J. Ewins, "Modal analysis and testing of rotating structures," *Philosophical Transactions of the Royal Society*, vol. 359, no. 1778, pp. 61–96, Jan. 2001.

[12] P. V. Overschee and B. D. Moor, *Subspace Identification for Linear Systems: Theory, Implementation, Applications*. Boston, MA: Kluwer, 1996.

[13] M. Basseville, A. Benveniste, M. Goursat, and L. Hermans, "Output-only subspace-based structural identification: From theory to industrial testing practice," *Journal of Dynamic Systems, Measurement, and Control*, vol. 123, no. 4, pp. 668–676, Dec. 2001.

[14] A. Lees, J. Sinha, and M. Friswell, "Model-based identification of rotating machines," *Mechanical Systems and Signal Processing*, vol. 23, no. 6, pp. 1884–1893, Aug. 2009.

[15] M. Basseville, A. Benveniste, B. Gach-Devauchelle, and M. Goursat, "In-situ damage monitoring in vibration mechanics: Diagnostics and predictive maintenance," *Mechanical Systems and Signal Processing*, vol. 7, no. 5, pp. 401–423, Sep. 1993.

[16] M. Basseville, A. Benveniste, M. Goursat, and L. Mevel, "In-flight vibration monitoring of aeronautical structures," *IEEE Control Systems*, vol. 27, no. 5, pp. 27–42, Oct. 2007.

[17] J. H. Weng, C. H. Loh, and J. N. Yang, "Experimental study of damage detection by data-driven subspace identification and finite-element model updating," *Journal of Structural Engineering*, vol. 135, no. 12, pp. 1533–1544, Dec. 2009.

[18] M. Basseville, M. Abdelghani, and A. Benveniste, "Subspace-based fault detection algorithms for vibration monitoring," *Automatica*, vol. 36, no. 1, pp. 101–109, Jan. 2000.

[19] T. Wolff and M. Richardson, "Fault detection in structures from changes in their modal parameters," in *Proceedings of the 7th International Modal Analysis Conference*, vol. 1, Las Vegas, NV, 1989, pp. 87–94.

[20] A. Benveniste, M. Basseville, and G. Moustakides, "The asymptotic local approach to change detection and model validation," *IEEE Transactions on Automatic Control*, vol. 32, no. 7, pp. 583–592, Jul. 1987.

[21] M. Basseville, "On-board component fault detection and isolation using the statistical local approach," *Automatica*, vol. 34, no. 11, pp. 1391–1415, Nov. 1998.

[22] Q. Zhang, M. Basseville, and A. Benveniste, "Early warning of slight changes in systems," *Automatica*, vol. 30, no. 1, pp. 95–113, Jan. 1994.

[23] L. Mevel, L. Hermans, and H. V. der Auweraer, "Application of a subspace-based fault detection method to industrial structures," *Mechanical Systems and Signal Processing*, vol. 13, no. 6, pp. 823–838, Nov. 1999.

[24] G. McDonald and Q. Zhao, "Model-based adaptive frequency estimator for gear crack fault detection," in *American Control Conference*, San Francisco, CA, 2011, pp. 792–797.

[25] W. Wang and A. K. Wong, "Autoregressive model-based gear fault diagnosis," *Journal of Vibration and Acoustics*, vol. 124, no. 2, pp. 172–179, Apr. 2002.

[26] S. Yang and Q. Zhao, "Real-time frequency estimation for sinusoidal signals with application to robust fault detection," *International Journal of Adaptive Control and Signal Processing*, vol. 27, no. 5, p. 386399, May 2013.

[27] R. T. Rato, M. D. Ortigueira, and A. G. Batista, "On the HHT, its problems, and some solutions," *Mechanical Systems and Signal Processing*, vol. 22, no. 6, pp. 1374–1394, Aug. 2008.

[28] Y. Lei, Z. He, and Y. Zi, "Application of the EEMD method to rotor fault diagnosis of rotating machinery," *Mechanical Systems and Signal Processing*, vol. 23, no. 4, pp. 1327–1338, May 2009.

[29] Y. Lei and M. J. Zuo, "Fault diagnosis of rotating machinery using an improved HHT based on EEMD and sensitive IMFs," *Measurement Science and Technology*, vol. 20, no. 12, pp. 125–701, Dec. 2009.

[30] F. N. Chowdhury, "Ordinary and neural chi-squared tests for fault detection in multioutput stochastic systems," *IEEE Transactions on Control Systems Technologies*, vol. 8, no. 2, pp. 372–379, Mar. 2000.